



ALMA MATER STUDIORUM
UNIVERSITÀ DI BOLOGNA

ARCHIVIO ISTITUZIONALE
DELLA RICERCA

Alma Mater Studiorum Università di Bologna
Archivio istituzionale della ricerca

Seismic surface wave attenuation by resonant metasurfaces on stratified soil

This is the final peer-reviewed author's accepted manuscript (postprint) of the following publication:

Published Version:

Zeng, C., Zhao, C., Zeighami, F. (2022). Seismic surface wave attenuation by resonant metasurfaces on stratified soil. *EARTHQUAKE ENGINEERING & STRUCTURAL DYNAMICS*, 51(5), 1201-1223 [10.1002/eqe.3611].

Availability:

This version is available at: <https://hdl.handle.net/11585/857268> since: 2024-07-03

Published:

DOI: <http://doi.org/10.1002/eqe.3611>

Terms of use:

Some rights reserved. The terms and conditions for the reuse of this version of the manuscript are specified in the publishing policy. For all terms of use and more information see the publisher's website.

This item was downloaded from IRIS Università di Bologna (<https://cris.unibo.it/>).
When citing, please refer to the published version.

(Article begins on next page)

1 **SEISMIC SURFACE WAVE ATTENUATION BY RESONANT METASURFACES ON**
2 **STRATIFIED SOIL**

3
4 **Chao Zeng¹, Chunfeng Zhao¹ and Farhad Zeighami²**

5 ¹School of Civil Engineering, Hefei University of Technology, Hefei 230009, China

6 ²Department of Civil, Chemical, Environmental and Materials Engineering - DICAM, University of Bologna,
7 Bologna 40136, Italy

8
9 **Correspondence**

10 Chunfeng Zhao, School of Civil Engineering, Hefei University of Technology, Hefei, Anhui, 230009, China

11 E-mail: zhaowindy@hfut.edu.cn

12
13 **Abstract**

14
15 This study aims to theoretically and numerically investigate the dispersion relations of Rayleigh waves propagating
16 through vertical oscillators periodically distributed on stratified media. The classical elastodynamics theory and an
17 effective medium approximation method are adopted to describe the dynamic behavior of metasurfaces and hybridization
18 between the local oscillators and the foundational surface wave modes. The Abo-zena algorithm and delta-matrix method
19 are combined to simplify the eigen equation to overcome the accuracy problem in solving the closed-form dispersion laws
20 and improve the computational efficiency. Subsequently, plane-strain finite element (FE) models with three configurations
21 are developed to confirm the analytical predictions and obtain further insight into the resonator-Rayleigh wave coupling
22 mechanism. The numerical results are in good agreement with the analytical solutions, revealing that only the foundational
23 mode is strongly coupled with the vertical resonators at resonance, while the surface wave band gap reported in
24 homogeneous media is crossed by the remaining higher-order surface modes. The attenuation performance and mechanical
25 behavior of a finite-length metasurface are investigated, and it is demonstrated that the output surface ground motion can
26 be significantly reduced in a narrow frequency band near resonance. Moreover, a graded resonant metasurface with
27 decreasing frequency is simulated to assess the feasibility of broadband attenuation. In summary, the aforementioned
28 analytical framework and numerical simulation results show that the vertical oscillators placed atop a stratified soil system
29 can be designed as resonant metasurfaces for shielding seismic surface waves to protect multiple large infrastructures or
30 special structures from earthquake hazards.

31
32 **KEYWORDS**

33
34 Resonant metasurfaces, Rayleigh waves, stratified soils, soil-resonator interaction, dispersion analysis, ground
35 vibration attenuation

36
37 **1 INTRODUCTION**

38
39 Synthetic periodic structures with periodic unit cells or local resonant inclusions, namely, phononic crystals and
40 elastic metamaterials, have been extensively studied to manipulate the propagation of acoustic and mechanical
41 waves at different scales, resulting in frequency band gaps wherein wave propagation is suppressed.¹ Therefore, the

42 engineered periodic structures are expected to be applied for wave filtering and waveguiding through approaches
43 that cannot be adopted in natural materials. In particular, the use of finite periodic structures to form elastic
44 metamaterials can generate exceptional effects, including dispersion properties,²⁻⁵ negative refraction,^{6,7} and
45 acoustic invisibility.^{8,9} These effects have been widely used in optics, acoustics, and elastic media at both microscale
46 and geophysical scales, such as superlensing,^{10,11} wave guiding,¹²⁻¹⁴ acoustic cloaking,¹⁵⁻¹⁷ elastic wave
47 obstacles,¹⁸⁻²⁰ and seismic wave mitigation.²⁰⁻²⁴

48
49 In 1987, Yablonovitch² and John³ first reported the discovery of band gaps in their study of the propagation of light
50 waves in periodic media. By introducing the concept of transformation optics in 2006, Leonhardt²⁵ and Pendry et
51 al.²⁶ popularized the technique, based on which metamaterials control wave propagation. This concept has been
52 applied at different geometric scales, ranging from nanometer-scale for thermal insulation²⁷ to meter-scale for
53 seismic wave isolation.²⁰⁻²⁴ For this reason, in the past two decades, many researchers have developed a variety of
54 novel passive isolation devices utilizing periodicity and local resonances in civil engineering. Cheng and Shi²⁸
55 innovatively constructed a new type of seismic isolation device called periodic foundation, where inclusions are
56 periodically embedded in matrix materials. Subsequently, Xiang²⁹ and Zhao et al.^{23,24} experimentally and
57 numerically analyzed the feasibility of a one-dimensional layered periodic foundation to attenuate longitudinal and
58 shear waves in the 0–50 Hz frequency range. The results revealed that both the horizontal and vertical dynamic
59 responses of the superstructure decreased noticeably when the excitation frequencies were within the band gaps.
60 Considering that the surface wave components in seismic excitation are more harmful to infrastructures, Brûlé et
61 al.²² conducted a large-scale experiment in which a meter-sized periodic array of cylindrical holes was used to shield
62 seismic surface waves, thereby mitigating ground vibration at frequencies of approximately 50 Hz. Analogous
63 conclusions were published by Miniaci et al.,²⁰ who numerically studied the attenuation performance of three
64 periodic configurations for low-frequency bulk and surface waves, showing that only periodic structures with a
65 lattice constant at decameter dimensions could generate band gaps below 10 Hz.

66
67 Conversely, locally resonant structures consisting of inclusions embedded in a matrix can interact with incident
68 waves at a sub-wavelength scale.^{1,5} Recently, researchers have proposed the feasibility of shielding surface seismic
69 waves by arranging a periodic array of resonators or barriers on the soil surface. A series of interesting studies
70 conducted by Colombi et al.³⁰ showed that the strong impedance mismatch and coupling of wave modes between
71 surface waves and an array of trees could generate surface wave hybridization band gaps at approximately 40 Hz.
72 Later, Colquitt and Colombi et al.^{31,32} reported the initial idea of vertical sub-wavelength resonators distributed on
73 infinite elastic half-space interacting with Rayleigh waves to mitigate surface ground motion, commonly known as
74 “resonant metasurfaces” from their seminal works. According to the local resonance mechanism, Palermo et al.³³
75 designed soil-embedded resonators to block seismic surface waves below 10 Hz and theoretically and
76 experimentally demonstrated the conversion of Rayleigh waves to shear bulk waves.

77
78 In addition, the heterogeneity of soil profile in practical engineering might induce elastic wave bending effects,
79 frequently indicated as the “mirage” effect.³⁴ To consider the effect of substrate material inhomogeneity, Palermo et
80 al.³⁵ numerically and experimentally investigated how sagittal polarized guided surface acoustic modes (GSAMs)
81 interact with surface resonances in unconsolidated granular media. Later, Zaccherini et al.³⁶ further revealed the
82 propagation and mitigation performance of Rayleigh-like waves in a granular medium equipped with multi-layer

83 sub-wavelength resonant metabarriers. Both the small-scale experiment and numerical simulation showed that the
84 low-order GSAM could be strongly coupled to the metasurfaces at resonance, while all higher-order surface acoustic
85 modes presented a down-conversion phenomenon, owing to the heterogeneity of the granular media. Moreover,
86 Zeighami and Palermo et al.³⁷ numerically designed a locally resonant metabarrier placed over a heterogeneous soil
87 surface to assess the attenuation performance of medium-size scale resonant barriers for seismic surface waves in
88 the range of 50–100 Hz.

89
90 To the best of the Authors' knowledge, due to the high cost of resonator preparation and soil excavation engineering,
91 the aforementioned studies mainly focused on describing the interaction of Rayleigh waves with vertical resonators
92 in semi-infinite space based on analytical models and numerical simulations, or emphasizing vertically hybrid
93 surface waves in inhomogeneous media through numerical analyses and small-scale experiments. In such case, some
94 practical engineering problems, such as real site conditions, the effect of hysteretic damping and soil nonlinearity
95 under dynamic excitations have not been fully considered so far. Although Pu et al.³⁸ have investigated the influence
96 of resonant metasurfaces and fluid–solid interaction on surface wave propagation under groundwater level variations,
97 an analytical framework for the coupling between Rayleigh waves and local resonators distributed on stratified soil
98 surfaces has not been reported on the geophysical scale. In this study, we aim to investigate (i) the analytical
99 solutions of the dispersion laws for local resonators placed atop a stratified soil surface, (ii) the interaction of
100 Rayleigh waves with vertically resonant metasurfaces, and (iii) the attenuation performance of finite-length resonant
101 metasurfaces.

102
103 The remainder of this paper is organized as follows. After reviewing the dynamic properties of periodic and locally
104 resonant structures, an analytical model of resonant metasurfaces under practical engineering conditions is proposed,
105 considering the propagation of Rayleigh waves through a stratified semi-infinite space equipped with local
106 resonators in Section 1. Based on the classical elastodynamic theory and an effective medium approach, the
107 dispersion equation of stratified soil–resonator interaction is derived in Section 2, and the eigen equation is
108 simplified by recombining the Abo-zena algorithm and delta matrix method to avoid the problem of high-frequency
109 effective digit loss. In Section 3, three types of unit cell FE models and transmission models with finite-length
110 metasurfaces are designed, and the validity of the FE model is verified by comparison with those proposed in
111 previous studies. In Section 4, to gain further insight into the resonator–surface wave coupling mechanism, the
112 theoretical dispersion laws of stratified soil–resonators are plotted and validated again based on FE simulations.
113 Additionally, the attenuation performance of finite-length metasurfaces is investigated in the frequency and time
114 domains. We subsequently design a graded resonant metasurface with decreasing frequency and compare their
115 isolation effectiveness with those of the reference models via time history analyses. Finally, concluding remarks are
116 presented in Section 5.

117
118 **Notation**

119

ρ	= density	C_L	= longitudinal wave velocity
d	= thickness		= $\sqrt{(\lambda + 2\mu) / \rho}$
λ, μ	= Lamé elastic constants	C_S	= shear wave velocity
f	= frequency		= $\sqrt{\mu / \rho}$

c	=	phase velocity of the free wave along the x -axis	γ_L	=	$\begin{cases} i\sqrt{(c/C_L)^2 - 1} & c > C_L \\ \sqrt{1 - (c/C_L)^2} & c < C_L \end{cases}$
u	=	x component of displacement	γ_S	=	$\begin{cases} i\sqrt{(c/C_S)^2 - 1} & c > C_S \\ \sqrt{1 - (c/C_S)^2} & c < C_S \end{cases}$
w	=	z component of displacement	γ	=	$2(C_S/c)^2$
σ_z	=	normal stress	P	=	$\exp(\gamma_L kd)$
τ_{xz}	=	tangential stress	Q	=	$\exp(\gamma_S kd)$
ω	=	$2\pi f$			
k	=	ω/c			
i	=	$\sqrt{-1}$			

120

121 2 ANALYTICAL FRAMEWORK

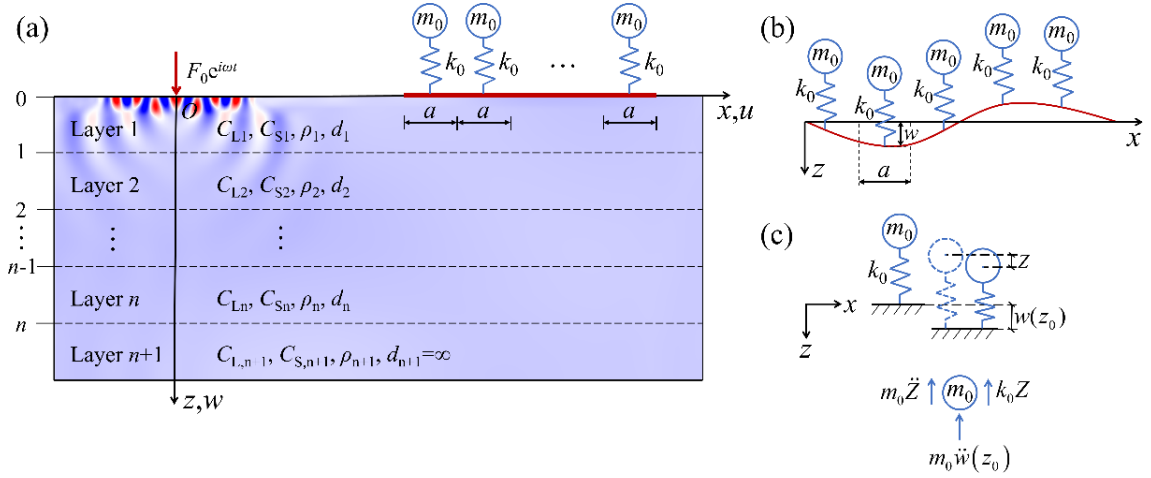
122

123 In this section, we develop an analytical framework to derive the dispersion equation of Rayleigh waves in stratified
 124 soils interacting with surface resonators, numerically and experimentally, to investigate sagittal polarized GSAMs in
 125 unconsolidated granular media interacting with vertical surface oscillators.³⁵ Accordingly, we restrict the
 126 investigation to a two-dimensional (2D) plane strain problem in the x - z plane (see Figure (1a)). Consider a
 127 horizontally stratified elastic semi-infinite space with surface waves propagating along the x -axis. Each layer is
 128 assumed to be isotropic, homogeneous, and perfectly bonded at the interface, and its geometric and physical
 129 properties are shown in Figure 1(a). Additionally, numerous previous studies^{30–33,35–38} have demonstrated that only
 130 the vertical resonance mode can open a significant surface wave band gap. Thus, the resonant metasurfaces are
 131 represented by a certain number of identical single-degree-of-freedom single mass–spring resonators in meter-size
 132 dimensions.

133

134 The dispersion laws of the hybrid Rayleigh waves are theoretically derived through an effective medium
 135 approximation and continuity of displacement and stress at the interface to guide the design of resonant
 136 metasurfaces. The procedures of the analytical framework are arranged as follows: (i) the displacements and stresses
 137 at the free surface caused by Rayleigh waves propagating in isotropic, linear elastic half-space, (ii) the dynamic
 138 response of a vertical oscillator subjected to harmonic base excitation, (iii) the eigen equation of Rayleigh waves
 139 interacting with surface resonators, and (iv) an improved algorithm for solving the eigen equation.

140



141
142
143
144
145
146

Figure 1. Schematic of the resonant metasurfaces. (a) Rayleigh waves interacting with surface resonators on stratified soils, with notations used in the theoretical model; (b) Physical model of the resonant metasurfaces; (c) Motion of representative single mass–spring resonator under vertical seismic excitation.

147 2.1 Waves motion in elastic media

148
149
150
151

The physical model is shown schematically in Figure 1(b). For isotropic, linear elastic media ignoring damping and body force, the governing equation of waves propagating in the soil substrate can be drawn by the displacement vector $\mathbf{u}(\mathbf{r})$:

$$(\lambda(\mathbf{r}) + \mu(\mathbf{r}))\nabla(\nabla \cdot \mathbf{u}(\mathbf{r})) + \mu\nabla^2 \mathbf{u}(\mathbf{r}) = \rho(\mathbf{r}) \frac{\partial^2 \mathbf{u}(\mathbf{r})}{\partial t^2}, \quad (1)$$

152 where $\nabla = [\partial / \partial x, \partial / \partial z]$ is the differential operator, $\mathbf{u}(\mathbf{r}) = [u, w]$ is the displacement vector, and t is the time.

153 According to the Helmholtz decomposition, the vertical and horizontal displacement components u and w of the
154 wave field can be expressed as

$$u = \frac{\partial \phi}{\partial x} - \frac{\partial \psi}{\partial z}, \quad w = \frac{\partial \phi}{\partial z} + \frac{\partial \psi}{\partial x}, \quad (2)$$

155 where ϕ and ψ are the scalar and vector potential functions of the dilatational and transverse components of the
156 displacement, respectively, and those for a semi-infinite elastic domain take the following form:^{39,40}

$$\nabla^2 \phi = \frac{1}{C_L^2} \frac{\partial^2 \phi}{\partial t^2}, \quad \nabla^2 \psi = \frac{1}{C_S^2} \frac{\partial^2 \psi}{\partial t^2}. \quad (3)$$

157
158
159

Assuming harmonic waves traveling along the x -axis with angular frequency ω and wavenumber k and recognizing that the waves are plane, the potential functions can be considered as

$$\phi(x, z, t) = \phi_0(z) \exp[i(\omega t - kx)], \quad (4a)$$

$$\psi(x, z, t) = \psi_0(z) \exp[i(\omega t - kx)]. \quad (4b)$$

160
161

Substituting Equation (4a) and (4b) into Equation (3) yields two uncoupled equations:

$$\frac{d^2\phi_0}{dz^2} = k^2 \left(1 - \frac{c^2}{C_L^2}\right) \phi_0, \quad (5a)$$

$$\frac{d^2\psi_0}{dz^2} = k^2 \left(1 - \frac{c^2}{C_S^2}\right) \psi_0. \quad (5b)$$

162 Solutions to Equation (5a) and (5b) are

$$\phi_0(z) = a_1 \exp(\gamma_L kz) + a_2 \exp(-\gamma_L kz) = \phi^+(z) + \phi^-(z), \quad (6a)$$

$$\psi_0(z) = b_1 \exp(\gamma_S kz) + b_2 \exp(-\gamma_S kz) = \psi^+(z) + \psi^-(z), \quad (6b)$$

163 where the four unknown constants a_1 , a_2 , b_1 , and b_2 appearing in Equation (6a) and (6b) are determined by the
 164 boundary conditions of each surface layer. For convenience, Equation (6a) and (6b) are expressed more concisely,
 165 where ϕ^+ and ψ^+ represent the up-going waves and ϕ^- and ψ^- represent the down-going waves.

166

167 Substituting Equation (6a) and (6b) into Equation (2) yields a set of equations relating the displacement components
 168 to ϕ^+ , ϕ^- , ψ^+ , and ψ^- as follows:

$$u = -ik\phi^+ - ik\phi^- - k\gamma_S\psi^+ + k\gamma_S\psi^-, \quad (7a)$$

$$w = k\gamma_L\phi^+ - k\gamma_L\phi^- - ik\psi^+ - ik\psi^-, \quad (7b)$$

169 from which the stresses σ_z and τ_{xz} can be expressed as follows:

$$\begin{aligned} \sigma_{zz} &= \lambda \nabla^2 \phi + 2\mu \frac{\partial^2 \phi}{\partial z^2} + 2\mu \frac{\partial^2 \psi}{\partial x \partial z} \\ &= \left[\lambda(k^2 \gamma_L^2 - k^2) + 2\mu k^2 \gamma_L^2 \right] \phi^+ + \left[\lambda(k^2 \gamma_L^2 - k^2) + 2\mu k^2 \gamma_L^2 \right] \phi^- , \\ &\quad - 2i\mu k^2 \gamma_S \psi^+ + 2i\mu k^2 \gamma_S \psi^- \end{aligned} \quad (8a)$$

$$\begin{aligned} \tau_{xz} &= \mu \left(2 \frac{\partial^2 \phi}{\partial x \partial z} + \frac{\partial^2 \psi}{\partial x^2} - \frac{\partial^2 \psi}{\partial z^2} \right) \\ &= \mu \left[-2ik^2 \gamma_L \phi^+ + 2ik\gamma_L \phi^- - (k^2 + k^2 \gamma_S^2) \psi^+ - (k^2 + k^2 \gamma_S^2) \psi^- \right], \end{aligned} \quad (8b)$$

170 where the factor $\exp[i(\omega t - kx)]$ is suppressed in Equation (7) and (8).

171

172 2.2 Dynamics of surface resonators

173

174 The kinematic equation of a single mass–spring resonator subjected to the base excitation is expressed as follows:

$$m_0 \left(\ddot{Z} + \ddot{w}(z_0) \right) + k_0 Z = 0, \quad (9)$$

175 where m_0 is the resonator mass, k_0 is the vertical spring stiffness, Z denotes the relative motion of the mass with
 176 respect to the ground, and $w(z_0)$ the base displacement (and both are supposed to be positive in the downward
 177 z -direction, see Figure 1(c)).

178

179 A harmonic wave solution of the form $Z = Z_0 \exp[i(\omega t - kx)]$ is assumed. Substituting the equation into Equation
 180 (9), we obtain the resonator displacement amplitude as follows:

$$Z_0 = \frac{\omega^2}{\omega_0^2 - \omega^2} w(z_0), \quad (10)$$

181 where ω_0 is the angular resonance frequency. The Rayleigh wavelength at the angular resonance frequency is much
 182 larger than the mass–spring spacing a , that is, the resonator and its footprint length have sub-wavelength dimensions
 183 at the resonance frequency. Thus, an effective medium approximation method is introduced to approximate the
 184 uniform vertical pressure stress σ_z exerted by the mass–spring at the surface ($z = 0$) as the elastic force divided by

185 the area of the resonator foundation.

$$\sigma_z(z_0) = \frac{k_0 Z}{A} = \frac{\omega^2 \omega_0^2 m_0}{A(\omega_0^2 - \omega^2)} w(z_0), \quad (11)$$

186 where A is the area of each resonator foundation. For the surface resonators arranged in a square lattice in this study,

$$187 \quad A = a^2.$$

188

189 2.3 Eigen equation

190

191 Moreover, Equation (7) and (8) can be written in the matrix notation as

$$\mathbf{S}(z) = \mathbf{H}\Phi(z), \quad (12)$$

192 where

$$\mathbf{S}(z) = \begin{bmatrix} iu & w & \frac{\sigma_{zz}}{k^2 c^2} & \frac{i\tau_{xz}}{k^2 c^2} \end{bmatrix}^T, \quad (13a)$$

$$\Phi(z) = \begin{bmatrix} \phi^+(z) & \phi^-(z) & -i\psi^+(z) & i\psi^-(z) \end{bmatrix}^T, \quad (13b)$$

193 and \mathbf{H} is a 4×4 matrix whose elements are a function of the elastic constants of the medium at each layer and phase
194 velocity c , and independent of the frequency f (see Appendix). Thus, Equation (12) can be applied to each layer.

195

196 For the m th layer, according to the displacement characteristics of each layer in the positive z -direction, the relation
197 between the four unknown coefficients at the boundary m and the boundary $m-1$ can be written as

$$\Phi_m(z_m) = \mathbf{E}_m \Phi_m(z_{m-1}), \quad (14)$$

198 where

$$\mathbf{E}_m = \text{diag} \left[P \quad \frac{1}{P} \quad Q \quad \frac{1}{Q} \right]_m, \quad z_0 = 0. \quad (15)$$

199

200 By substituting Equation (12) into Equation (14), the stress displacement vector can be expressed as

$$\begin{aligned} \mathbf{S}_m(z_m) &= \mathbf{H}_m \mathbf{E}_m \Phi_m(z_{m-1}) = \mathbf{H}_m \mathbf{E}_m \mathbf{H}_m^{-1} \mathbf{S}_m(z_{m-1}), \\ &= \mathbf{T}_m \mathbf{S}_m(z_{m-1}) \end{aligned} \quad (16)$$

201 where

$$\mathbf{T}_m = \mathbf{H}_m \mathbf{E}_m \mathbf{H}_m^{-1}. \quad (17)$$

202

203 Owing to the continuity of the stress displacement vector at the boundary of any layer, Equation (16) can be further
204 expressed as:

$$\mathbf{S}(z_n) = \mathbf{T}_n \mathbf{T}_{n-1} \cdots \mathbf{T}_1 \mathbf{S}(z_0) = \mathbf{K} \mathbf{S}(z_0), \quad (18)$$

205 where

$$\mathbf{K} = \mathbf{T}_n \mathbf{T}_{n-1} \cdots \mathbf{T}_1. \quad (19)$$

206

207 By substituting Equation (12) into Equation (18), we obtain

$$\Phi_{n+1}(z_n) = \mathbf{H}_{n+1}^{-1} \mathbf{K} \mathbf{S}(z_0) = \mathbf{R} \mathbf{S}(z_0), \quad (20)$$

208 where

$$\mathbf{R} = \mathbf{H}_{n+1}^{-1} \mathbf{K}. \quad (21)$$

209

210 Equipped with the interaction of the surface wave with the resonators, the stress-free boundary condition for the
 211 semi-infinite medium is substituted with the vertical stress σ_z . In addition, there is no source at infinity, i.e.,
 212 $\phi_{n+1}^+(z_n) = \psi_{n+1}^+(z_n) = 0$. Thereafter, Equation (20) becomes

$$\begin{bmatrix} 0 \\ \phi_{n+1}^-(z_n) \\ 0 \\ i\psi_{n+1}^-(z_n) \end{bmatrix} = \begin{bmatrix} r_{11} & r_{12} & r_{13} & r_{14} \\ r_{21} & r_{22} & r_{23} & r_{24} \\ r_{31} & r_{32} & r_{33} & r_{34} \\ r_{41} & r_{42} & r_{43} & r_{44} \end{bmatrix} \begin{bmatrix} \frac{i u(z_0)}{k} \\ \frac{w(z_0)}{k} \\ \frac{\xi w(z_0)}{k} \\ 0 \end{bmatrix}, \quad (22)$$

213 where $\xi = \frac{k\omega_0^2 m_0}{A(\omega^2 - \omega_0^2)}$, r_{ij} is the element of the matrix \mathbf{R} .

214
 215 By arranging the first and third equations in Equation (22), we obtain

$$\begin{cases} r_{11} \frac{i u(z_0)}{k} + [r_{12} + \xi r_{13}] \frac{w(z_0)}{k} = 0 \\ r_{31} \frac{i u(z_0)}{k} + [r_{32} + \xi r_{33}] \frac{w(z_0)}{k} = 0 \end{cases}. \quad (23)$$

216 To obtain the nontrivial solutions of Equation (23), the coefficient matrix \mathbf{LS} can be calculated as

$$\det[\mathbf{LS}] = \begin{vmatrix} r_{11} & r_{12} + \xi r_{13} \\ r_{31} & r_{32} + \xi r_{33} \end{vmatrix} = 0. \quad (24)$$

217
 218 **2.4 Improved matrix formulation**

219
 220 The eigen equations derived thus far constitute a closed-form solution to the problem, and a concise algorithm can
 221 be developed on this basis. Numerically, however, the coefficient matrix \mathbf{LS} was unsatisfactory. The research results
 222 of Knopoff,⁴¹ Dunkin,⁴² and Thrower et al.⁴³ showed that there were serious precision difficulties in determining all
 223 the real roots of the characteristic determinant for a layered elastic half-space, and they proposed to overcome this
 224 problem by introducing a delta matrix algorithm. Additionally, Abo-zena⁴⁴ developed another method that not only
 225 avoids the persistent problem of loss of effective digits at high frequencies, but also improves the convergence speed.
 226 Accordingly, we improve the Abo-zena algorithm and delta matrix method to determine the hybrid Rayleigh wave
 227 dispersion of layered elastic medium without restriction on the loss of high-frequency effective digits, ensuring a
 228 higher computational efficiency.

229
 230 As is evident, \mathbf{LS} is only a 2×2 matrix formed by multiplying the first and third rows of the matrix \mathbf{H}_{n+1}^{-1} and the
 231 first three columns of matrix \mathbf{K} . Therefore, the first and third rows of the matrix \mathbf{H}_{n+1}^{-1} can be denoted as

$$\begin{bmatrix} \mathbf{E}_A \\ \mathbf{E}_B \end{bmatrix} = \frac{1}{2} \begin{bmatrix} \gamma & -\frac{(\gamma-1)}{\gamma_L} & -\frac{1}{\rho} & -\frac{1}{\rho\gamma_L} \\ -\frac{(\gamma-1)}{\gamma_S} & \gamma & \frac{1}{\rho\gamma_S} & -\frac{1}{\rho} \end{bmatrix}. \quad (25)$$

232 Thereafter, the matrix \mathbf{LS} can be expressed as

$$\mathbf{LS} = \begin{bmatrix} \mathbf{E}_A \\ \mathbf{E}_B \end{bmatrix} \mathbf{K} \begin{bmatrix} 1 & 0 \\ 0 & 1 \\ 0 & \xi \\ 0 & 0 \end{bmatrix} = \begin{bmatrix} \begin{bmatrix} \mathbf{E}_A \mathbf{K} \\ 0 \\ 0 \\ 0 \end{bmatrix} & \begin{bmatrix} 1 \\ 0 \\ 0 \\ 0 \end{bmatrix} \\ \begin{bmatrix} \mathbf{E}_B \mathbf{K} \\ 0 \\ 0 \\ 0 \end{bmatrix} & \begin{bmatrix} \xi \\ 1 \\ \xi \\ 0 \end{bmatrix} \end{bmatrix}, \quad (26)$$

233 from which Equation (24) can be rewritten as

$$\det[\mathbf{LS}] = \begin{bmatrix} \mathbf{E}_A \mathbf{K} \\ 0 \\ 0 \\ 0 \end{bmatrix} \begin{bmatrix} 1 \\ 0 \\ \xi \\ 0 \end{bmatrix} - \begin{bmatrix} \mathbf{E}_A \mathbf{K} \\ 1 \\ \xi \\ 0 \end{bmatrix} \begin{bmatrix} 1 \\ 0 \\ 0 \\ 0 \end{bmatrix}. \quad (27)$$

234 Using the transpose property of the matrix, we can obtain the eigen determinant as

$$\det[\mathbf{LS}] = [1 \ 0 \ 0 \ 0] \mathbf{K}^T \left\{ [\mathbf{E}_A]^T [\mathbf{E}_B] - [\mathbf{E}_B]^T [\mathbf{E}_A] \right\} \mathbf{K} \begin{bmatrix} 0 \\ 1 \\ \xi \\ 0 \end{bmatrix}. \quad (28)$$

235

236 The related matrix can be further defined as $\mathbf{Y}_{n+1} = [\mathbf{E}_A]^T [\mathbf{E}_B] - [\mathbf{E}_B]^T [\mathbf{E}_A]$. More specifically,

$$\mathbf{Y}_{n+1} = \frac{1}{4} \begin{bmatrix} 0 & \gamma^2 - \frac{(\gamma-1)^2}{\gamma_L \gamma_s} & \frac{1}{\rho \gamma_s} & -\frac{\gamma}{\rho} + \frac{\gamma-1}{\rho \gamma_L \gamma_s} \\ -\gamma^2 + \frac{(\gamma-1)^2}{\gamma_L \gamma_s} & 0 & -\frac{\gamma-1}{\rho \gamma_L \gamma_s} + \frac{\gamma}{\rho} & -\frac{1}{\rho \gamma_L} \\ -\frac{1}{\rho \gamma_s} & \frac{\gamma-1}{\rho \gamma_L \gamma_s} - \frac{\gamma}{\rho} & 0 & \frac{1}{\rho^2} - \frac{1}{\rho^2 \gamma_L \gamma_s} \\ \frac{\gamma}{\rho} - \frac{\gamma-1}{\rho \gamma_L \gamma_s} & \frac{1}{\rho \gamma_L} & -\frac{1}{\rho^2} + \frac{1}{\rho^2 \gamma_L \gamma_s} & 0 \end{bmatrix}. \quad (29)$$

237 By substituting Equations (29) and (19) into Equation (28), we obtain

$$\det[\mathbf{LS}] = [1 \ 0 \ 0 \ 0] \mathbf{T}_1^T \cdots \mathbf{T}_{n-1}^T \mathbf{T}_n^T \mathbf{Y}_{n+1} \mathbf{T}_n \mathbf{T}_{n-1} \cdots \mathbf{T}_1 \begin{bmatrix} 0 \\ 1 \\ \xi \\ 0 \end{bmatrix}. \quad (30)$$

238 Equation (30) can be expressed in a recursive format equivalent to

$$\mathbf{Y}_m = \mathbf{T}_m^T \mathbf{Y}_{m+1} \mathbf{T}_m \quad n, n-1, \dots, 1, \quad (31a)$$

$$\det[\mathbf{LS}] = \mathbf{Y}_1(1,2) + \xi \mathbf{Y}_1(1,3), \quad (31b)$$

239 where $\mathbf{Y}_1(1,2)$ and $\mathbf{Y}_1(1,3)$ represent the elements of row1, column2, and row1, column3, respectively, in matrix \mathbf{Y}_1 .

240 From Equation (29), it follows that \mathbf{Y}_{n+1} is an antisymmetric matrix; if \mathbf{Y}_{n+1} is antisymmetric, then $\mathbf{T}_m^T \mathbf{Y}_{m+1} \mathbf{T}_m$ is

241 also antisymmetric.

242

243 This indicates that the above recursive formulas still cannot overcome the loss of significant digits. Additionally,

244 because there are only six independent elements in the matrix \mathbf{Y}_m , Equation (31a) can be arranged in terms of
 245 operations on the matrix elements:

$$\hat{y}_{ij} = \sum_{l=1}^4 \sum_{n=1}^4 g_{li} y_{ln} g_{nj}, \quad (32)$$

246 where \hat{y}_{ij} , g_{li} , and y_{ln} are the elements of the matrix \mathbf{Y}_m , \mathbf{T}_m , and \mathbf{Y}_{m+1} , respectively. According to the
 247 property of the antisymmetric matrix, Equation (32) can be expressed as:

$$\begin{aligned} \hat{y}_{ij} = & (g_{1i}g_{2j} - g_{2i}g_{1j})y_{12} + (g_{1i}g_{3j} - g_{3i}g_{1j})y_{13} + (g_{1i}g_{4j} - g_{4i}g_{1j})y_{14} + (g_{2i}g_{3j} - g_{3i}g_{2j})y_{23} \\ & + (g_{2i}g_{4j} - g_{4i}g_{2j})y_{24} + (g_{3i}g_{4j} - g_{4i}g_{3j})y_{34}. \end{aligned} \quad (33)$$

248 Equation (33) can be written in vector form:

$$\mathbf{W}_m = \mathbf{W}_{m+1} \mathbf{T}_m^* \quad m = n, n-1, \dots, 1, \quad (34)$$

249 where $\mathbf{W}_m = [\hat{y}_{12} \quad \hat{y}_{13} \quad \hat{y}_{14} \quad \hat{y}_{23} \quad \hat{y}_{24} \quad \hat{y}_{34}]$ and $\mathbf{W}_{m+1} = [y_{12} \quad y_{13} \quad y_{14} \quad y_{23} \quad y_{24} \quad y_{34}]$. From the expression
 250 of the elements of the matrix \mathbf{T}_m^* in Equation (33), it can be observed that each element of the matrix \mathbf{T}_m^* is a $2 \times$
 251 2 sub-determinant of the matrix \mathbf{T}_m , i.e., \mathbf{T}_m^* refers to the delta matrix of \mathbf{T}_m .

252

253 Considering the property of the delta matrix, the matrix \mathbf{T}_m^* can be expressed as

$$\mathbf{T}_m^* = \mathbf{H}_m^* \mathbf{E}_m^* (\mathbf{H}_m^{-1})^*, \quad (35)$$

254 where \mathbf{H}_m^* , \mathbf{E}_m^* , and $(\mathbf{H}_m^{-1})^*$ represent the delta matrices of \mathbf{H}_m , \mathbf{E}_m , and \mathbf{H}_m^{-1} , respectively.

255

256 By substituting Equation (35) into Equation (34), we obtain the system

$$\mathbf{W}_m = \frac{1}{4} \mathbf{W}_{m+1} \mathbf{H}_m^* \mathbf{E}_m^* (\mathbf{H}_m^{-1})^* \quad m = n, n-1, \dots, 1, \quad (36)$$

257 where the initial vector \mathbf{W}_m in Equation (36) can be expressed as

$$\mathbf{W}_{n+1} = \left[\gamma^2 - \frac{(\gamma-1)^2}{\gamma_L \gamma_s} \quad \frac{1}{\rho \gamma_s} \quad -\frac{\gamma}{\rho} + \frac{\gamma-1}{\rho \gamma_L \gamma_s} \quad \frac{\gamma}{\rho} - \frac{\gamma-1}{\rho \gamma_L \gamma_s} \quad -\frac{1}{\rho \gamma_L} \quad \frac{1}{\rho^2} - \frac{1}{\rho^2 \gamma_L \gamma_s} \right]_{n+1}. \quad (37)$$

258 Therefore, the characteristic Equation (31b) can be further written as

$$\mathbf{W}_1(1,1) + \xi \mathbf{W}_1(1,2) = 0, \quad (38)$$

259 where $\mathbf{W}_1(1,1)$ and $\mathbf{W}_1(1,2)$ represent the elements of row1, column1, and row1, column2, respectively, in matrix
 260 \mathbf{W}_1 . Incidentally, if n is set to zero, Equation (38) is reduced to the dispersion relation of the interaction between the
 261 resonant metasurfaces and Rayleigh waves propagating in an idealized elastic half-space.³³

$$\left(\frac{\omega^2}{\omega_0^2} - 1\right) \left[\left(2 - \frac{\omega^2}{k^2 C_s^2}\right)^2 - 4 \sqrt{1 - \frac{\omega^2}{k^2 C_L^2}} \sqrt{1 - \frac{\omega^2}{k^2 C_s^2}} \right] = \frac{\omega^4 m_0}{A \rho k^3 C_s^4} \sqrt{1 - \frac{\omega^2}{k^2 C_L^2}} \quad (39)$$

262

263 3 FE MODEL AND VALIDATION

264

265 Before proceeding with any numerical simulation related to the dispersion of stratified soil, it is necessary to choose
 266 the appropriate site condition characterizing the mechanical properties of each soil stratum. Cai et al.⁴⁵ have reported
 267 the attenuation performance of 1D layered periodic trenches embedded in stratified soil and its application in
 268 train-induced ground vibration damping. Thus, the depth-dependent speed profiles were considered in this study, as
 269 shown in Table 1.

270

271 Moreover, three types of 2D unit cell FE models and a transmission calculation model, developed in COMSOL

272 Multiphysics, were designed to confirm the analytical dispersion relation and obtain further insights into the
 273 resonator–surface wave coupling mechanism. Accordingly, we first verified the accuracy of the Bloch-wave FE
 274 method by comparing it with the numerical results published by Palermo et al.⁴⁶ Furthermore, the attenuation of
 275 surface waves inside the frequency band gap was also validated by performing a transmission analysis of an array of
 276 metasurfaces distributed on the surface of the ground in the frequency domain.

277
 278
 279

Table 1. Soil stratification and mechanical parameters.⁴⁵

No.	Soil type	Thickness d (m)	Density ρ (kg/m ³)	Shear speed C_S (m/s)	wave Longitudinal speed C_L (m/s)
1	Miscellaneous fill	4.6	1810	80.92	40.76
2	Plasticized silty clay	6.0	1850	117.99	60.71
3	Hard-plasticized granite residual soil	3.4	1950	125.05	65.62
4	Completely weathered granite	16.8	2100	121.89	70.37
5	Strongly weathered granite	9.2	2200	126.77	74.15

280
 281
 282

3.1 Unit cell design

283 Three configurations of the FE model were considered in the dispersion analysis: a stratified soil system with a
 284 stress-free boundary condition (BC) at the top, labeled as Unit cell A; a portion of homogeneous soil coupled with
 285 point mass–spring resonators, denoted as Unit cell B; and a unit cell C of the stratified soil–resonator interaction.
 286 For the stratified soil system (see Figure 2(a)), the unit cell has a width $w = a/10$ and a height $h = 40$ m to accurately
 287 identify surface wave modes around the resonant frequency. The soil stratification and mechanical parameters are
 288 provided in Table 1. In the numerical simulation, the unit cell substrate domain was discretized into triangular
 289 elements with quadratic Lagrange shape functions. In addition, we used the discretization of 10 elements for the
 290 minimum wavelength at the highest frequency of interest,^{47,48} that is, $d_{\min} = C_R / f_{\max} / 10$, where C_R is the
 291 Rayleigh velocity and f_{\max} is the highest frequency of interest in this study.

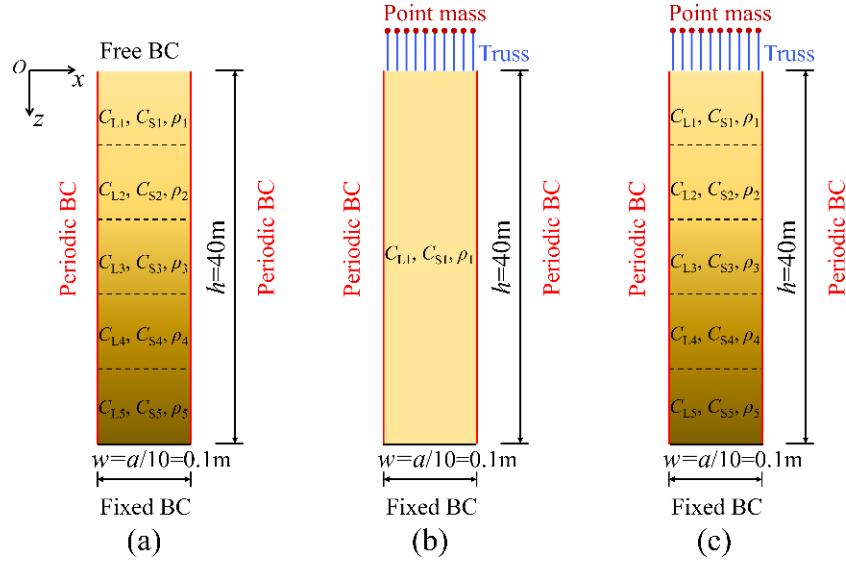
292
 293
 294
 295
 296
 297
 298
 299

Owing to the periodicity of the model, Bloch–Floquet BCs were applied to the lateral edges of the unit cell to
 simulate an infinite array of the stratified soil system along the direction of wave propagation and fixed BCs to the
 bottom edge to avoid undesired rigid motions. It is observed that the dispersion relation is an implicit function of the
 wavenumber k and eigen frequency f . The corresponding eigen frequency can be solved based on the FE approaches
 reported by Phani et al.⁴⁹ by changing across the wave numbers in the boundary of the first irreducible Brillouin
 zone. Thereafter, a post-processing method reported by Huang et al.⁵⁰ is implemented to automatically identify the
 numerical surface wave solutions from all the Bloch modes.

300
 301
 302
 303

The Unit cell B and C (see Figure 2(b) and (c)) have the same geometric size and mesh quality attributes as Unit cell
 A, except for the substitution of the standard zero-stress BCs with the previously discussed metasurface stresses. To
 simulate the uniform vertical stress imposed on the resonator foundation, a single mass–spring resonator was

304 dispersed over a set of 10 truss elements, as described in Ref 46, resulting in each point mass $m_t = m_0/100$ and
 305 Young's modulus of each truss $E = \omega_0^2 m_0 / S / 100$, where S is the cross-sectional area of the truss element.
 306 Additional point masses are also used to model the resonator mass borne by each truss element.
 307



308 (a) (b) (c)
 309
 310 **Figure 2. Schematic of unit cell FE model for dispersion analysis. (a) A stratified soil system with free BC at**
 311 **the top; (b) A homogeneous soil system coupled with a set of single mass–spring resonators; (c) A stratified**
 312 **soil system coupled with a set of single mass–spring resonators.**

314 3.2 Transmission model design

316 A 2D strip model with a finite array of resonators under plane-strain conditions was developed to assess the
 317 attenuation efficiency of the resonant metasurfaces placed atop a stratified soil surface, as schematically shown in
 318 Figure 3. When the surface waves propagate in the first-layered soil, the velocity of the Rayleigh waves can be
 319 approximated as $C_R \approx (0.87+1.12\nu) C_S / (1+\nu) = 38 \text{ m/s}$. The frequency range for frequency domain analysis is 1–10
 320 Hz. Therefore, the Rayleigh wavelength for the first-layered soil at the resonance frequency is expressed as $\lambda_{\omega R} = C_R$
 321 $/ f_0$, where f_0 is the resonance frequency of the resonator. The computational domain has a depth of $5 \lambda_{\omega R}$ and a total
 322 length of $18 \lambda_{\omega R} + 2 l_{\text{bar}}$, where l_{bar} represents the distribution length of the metasurfaces. The incident surface wave
 323 was generated by applying a vertical harmonic displacement ($w(f) = w_0 e^{i\omega t}$, $w_0 = 0.01\text{m}$). It should be emphasized
 324 that the source displacement generates both Rayleigh waves traveling along the free surface and bulk waves in the
 325 soil substrate, but the surface displacements in the far-field are dominated by Rayleigh waves, ensuring surface wave
 326 interaction with surface resonators.

327
 328 Triangular elements with quadratic Lagrange shape functions were also applied to discretize the field domain, and
 329 the mesh quality was consistent with the unit cell FE model. To avoid numerical oscillation near the resonance
 330 frequency, all the elements were assigned a small isotropic loss factor (that is, $\zeta = 0.05$). Additionally, perfectly

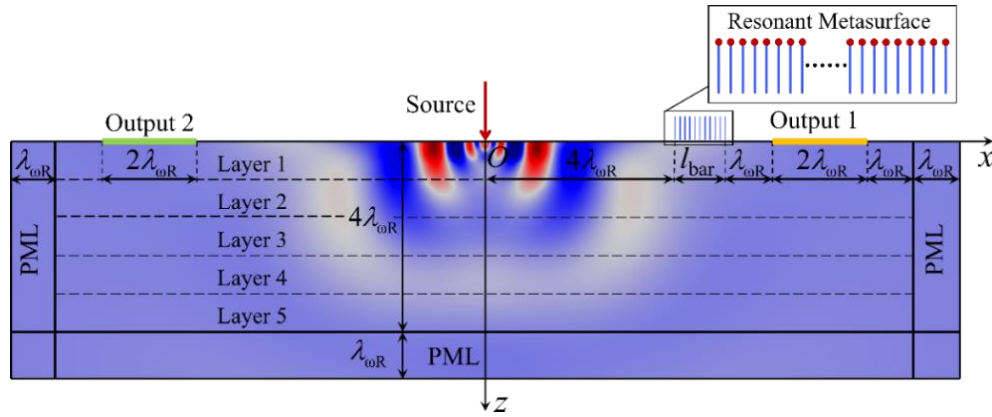
331 matched layers (PMLs) were employed at both the lateral and the bottom of the substrate to prevent undesired
 332 reflections from the domain boundaries.

333
 334 To evaluate the attenuation effect of the metasurfaces, the acceleration reduction spectrum (ARS) is defined as

$$\text{ARS} = 20 \log_{10} \frac{\int_0^{2\lambda_{\text{or}}} |a_{z,\text{with}}| dx}{\int_0^{2\lambda_{\text{or}}} |a_{z,\text{without}}| dx}, \quad (40)$$

335 where $a_{z,\text{with}}$ represents the vertical acceleration component extracted from output1, $a_{z,\text{without}}$ is the reference
 336 acceleration field obtained from the left side of the domain (Output2). Note that the ARS is negative if $a_{z,\text{with}}$ is less
 337 than $a_{z,\text{without}}$ that indicates that metasurfaces mitigate the ground vibration.

338



339

340

341 **Figure 3. Schematic of the 2D plane-strain FE model geometry. The computational domain on the right**
 342 **represents a finite number of mass–spring resonators attached to the free surface of a stratified soil system,**
 343 **while that on the left represents surface waves propagating along the free surface subjected to harmonic**
 344 **excitation.**

345

346 3.3 Comparison and validation

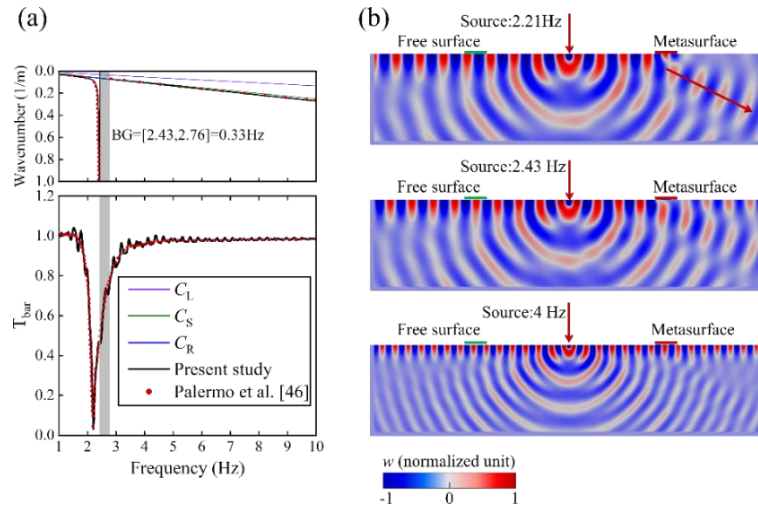
347

348 To substantiate the feasibility of the FE models, the problem of surface waves interacting with resonant metabarriers
 349 reported by previous researchers is reconsidered.⁴⁶ The upper panel of Figure 4(a) shows the dispersion curves for
 350 sedimentary soil coupled with a single-mass metabarrier. The unit cell has a width $w = A/(1m)/10$ and a height $h =$
 351 $4\lambda_{\text{or}}$, where λ_{or} is the Rayleigh wavelength at $f = 2.43$ Hz. The relationship between the transmission coefficient and
 352 excitation frequency obtained in this study was also compared with that in previous research, as depicted in the
 353 lower panel of Figure 4(a). In transmission analysis, the considered metabarrier has a length $L_{\text{res}} = \lambda_{\text{or}}$, with resonator
 354 mass $m = 10500$ kg and resonance frequency $f_r = 2.43$ Hz. Evidently, the surface wave dispersion curves and
 355 transmission spectra obtained in the present study agree well with those in previous studies.

356

357 Furthermore, it should be noted that the attenuation peak of the transmission spectrum deviates from the surface
 358 wave band gap (gray shaded area) and appears in the frequency region below the resonance frequency, where the
 359 surface waves are strongly hybridized with the resonant metabarrier. Figure 4(b) displays the nephogram of the

360 vertical displacement field generated by harmonic excitation at 2.21 Hz, 2.43 Hz, and 4 Hz. Apparent mode
 361 conversion of Rayleigh waves into bulk shear waves is observed at the frequency corresponding to the attenuation
 362 peak (2.21 Hz) that again validates the accuracy of the FE model. This phenomenon is further discussed in Section
 363 4.
 364



365
 366
 367 **Figure 4. Comparative study of dispersion laws and transmission spectra of surface waves interacting with**
 368 **resonators arranged on homogeneous soil surface. (a) Dispersion curves and corresponding acceleration**
 369 **reduction spectrum; (b) The nephogram of vertical displacement field generated by harmonic excitation at**
 370 **2.2 Hz, 2.43 Hz, and 4 Hz.**

371
 372 **4 RESULTS AND DISCUSSION**
 373 **4.1 Dispersion analysis**

374
 375 According to the mechanical parameters in Table 1, the first three-order surface wave modes (frequency versus
 376 wave number) of Unit cell A in the range of 1–10 Hz are theoretically and numerically calculated (see Figure 5(a)),
 377 along with the dispersion curves in terms of phase velocity versus frequency, as plotted in Figure 5(b). Note that the
 378 theoretical dispersion curves that are solutions of Equation (40) (that is, $\zeta = 0$), are shown as solid lines in three
 379 colors (for example, M1–M3), while solid pink circles represent the FE surface wave solutions. As reported by
 380 Graff,³⁹ multiple surface modes are induced by the presence of stress-free BC and inhomogeneous elastic properties
 381 of the stratified soil system. Additionally, the analytical solutions show excellent agreement with the numerical
 382 results, confirming the accuracy of the Bloch-wave FE approach again.
 383

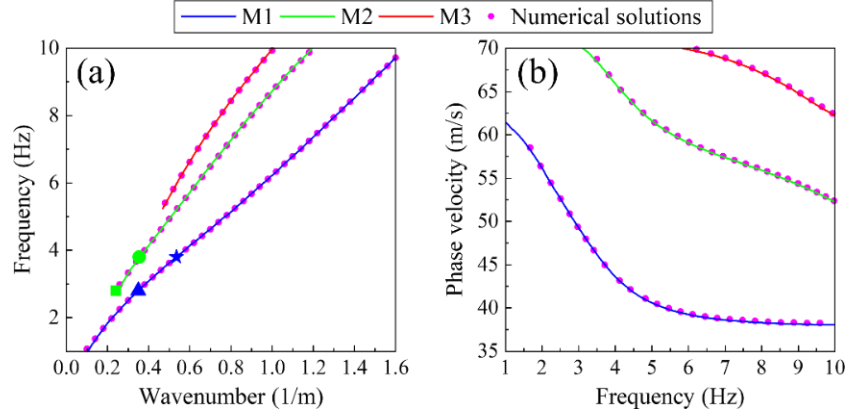


Figure 5. Dispersion curves for Unit cell A in terms of (a) frequency versus wavenumber and (b) phase velocity versus frequency.

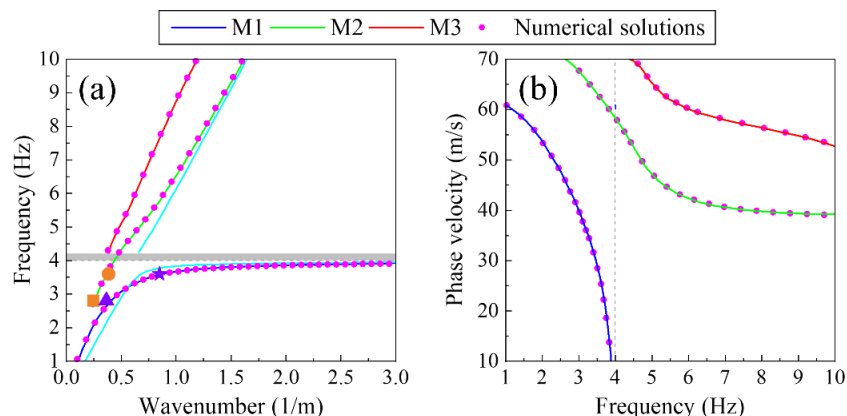
The dispersion curves for vertically polarized surface waves in a stratified soil system are displayed, and the mechanical parameters of the soil and surface resonator are specified in Table 1 and Table 2, respectively. It should be noted that each resonance frequency f_0 of the resonator is crucial for the mitigation of surface seismic waves below 10 Hz that cover the most energetic frequencies of seismic spectra. Specifically, for a mass of m_0 and resonant frequency f_0 , the compression stiffness of each resonator is $k_0 = m_0(2\pi f_0)^2$. Figure 6(a) and (b) show the analytical dispersion curves and FE solutions for Unit cell C in terms of frequency versus wavenumber and phase velocity versus frequency, respectively. This indicates that the FE solutions agree well with the analytical predictions. The vertical resonance of the resonator is plotted in Figure 6 by the gray dashed line. The first insight into the main features of the dispersion curves indicates that a highly localized mode (that is, M1) arises because of the coupling between Rayleigh waves and the metasurfaces, resulting in a flat dispersive branch at the resonance of the vertical resonator.

To emphasize the localization mechanism induced by the heterogeneous elastic properties, the analytical dispersion curves of a homogeneous soil system coupled with a resonant metasurface (Unit cell B), denoted by the solid cyan line, are also superimposed in Figure 6 (a). The mechanical parameters of the homogeneous soil are derived from the first layer in Table 1. It is observed that the Rayleigh waves in infinite elastic half-space hybridize with the vertical resonators at resonance, exhibiting a characteristic “avoided crossing” behavior. The dispersion curves are split into two repelling branches around the resonance frequency that results in a narrow surface wave band gap, as depicted in the gray area in Figure 6 (a). Within the frequency band gap, the propagation of Rayleigh waves is mitigated, and surface waves deviate from the stress-free surface in the form of shear vertically polarized waves, similar to what was observed in previous studies.^{33,46} However, this behavior is not observed in the case of stratified soil configuration. Although the presence of vertical oscillators results in a flat branch for the first-order surface modes of a stratified soil system that is akin to the lower branch of a homogeneous soil system, the surface wave band gap is permeated by higher-order surface modes, that is, the frequency band gap disappears.

Table 2. Mechanical parameters of the surface resonator.

Parameter	Value
Mass, m_0	400 kg
Stiffness, k_0	2.5266×10^5 N/m
Resonance frequency, f_0	4 Hz
Lattice constant, a	1 m

416



417

418

419 **Figure 6. Dispersion curves for Unit cell C in terms of (a) frequency versus wavenumber and (b) phase**
 420 **velocity versus frequency. The superimposed solid cyan lines in panel (a) are the dispersion curves of a**
 421 **homogeneous soil system coupled with resonant metasurfaces.**

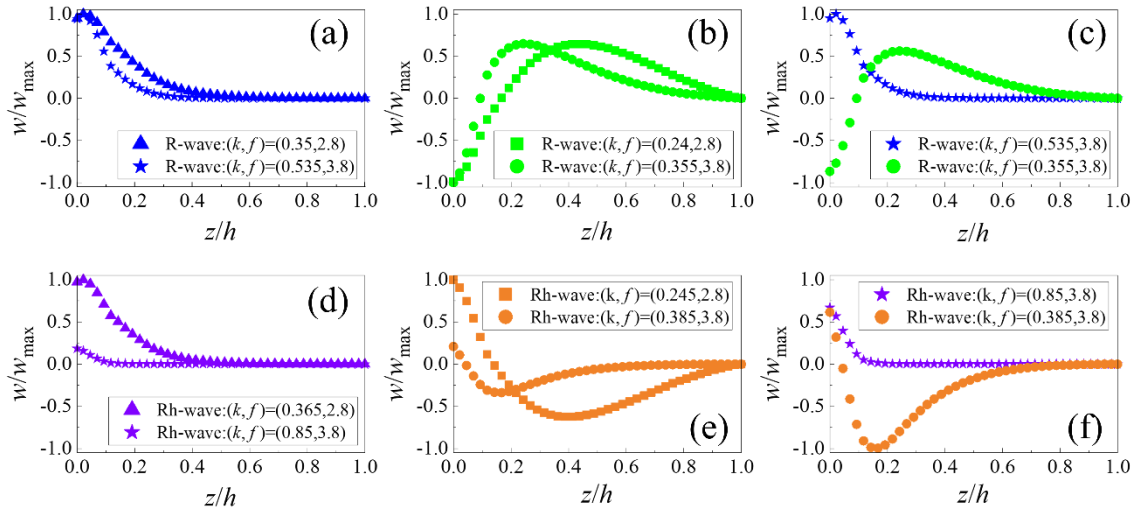
422

423 For this reason, the normalized vertical displacement amplitudes of Unit cell A and C changing with the depth
 424 profile below the resonance frequency were extracted to emphasize the hybridization degree of surface waves by the
 425 metasurfaces, as plotted in Figure 7. The vertical displacement data at different frequency–wavenumber values are
 426 extracted from the dispersion curves in Figure 5(a) and Figure 6(a), where the Rayleigh (R) and hybrid Rayleigh (Rh)
 427 wave shapes represent the surface waves propagating in Unit cell A and C, respectively. The vertical displacement
 428 amplitude of the first-order R-wave at different frequency wavenumbers does not change significantly, and the trend
 429 of the attenuation changes with depth is basically the same. In contrast, the vertical displacement of the Rh-wave
 430 near the resonance frequency (that is, $(k, f) = (0.85, 3.8)$) is confined to a thin layer, and the amplitude decays rapidly
 431 with depth further away from the free surface. Similar results (see Figure 7(b) and (e)) can be seen from the vertical
 432 displacement distribution of the second-order R-wave and Rh-wave along the depth. It can be asserted that such a
 433 phenomenon is the result of hybridization between the fundamental surface mode and metasurfaces that interact with
 434 an inhomogeneous elastic medium and gradually restrict the energy to the near-surface.

435

436 To investigate the coupling level of each order of surface modes with the metasurfaces, the vertical displacement
 437 fields of the first two order R and Rh waves close to the resonance frequency (that is, $f = 3.8$ Hz) were also
 438 compared, as shown in Figure 7(c) and (f). As shown in Figure 7(c), the vertical displacement amplitudes of the two
 439 modes are similar at the free surface, but the vertical displacement component of the first-order mode decays faster
 440 in the perpendicular direction than that of the second-order mode. Similar results can be observed in Figure 7(f). It
 441 can be concluded that only the fundamental surface mode can strongly couple to the resonant metasurfaces owing to
 442 the significant disappearance of the vertical displacement component at the free surface. Thus, it can be predicted

443 that these higher-order modes do no affect on the surface wave attenuation near the resonance frequency of
 444 metasurfaces.
 445



446
 447
 448 **Figure 7. Normalized vertical displacement amplitude of surface modes of Unit cell A and C changing with**
 449 **depth.**

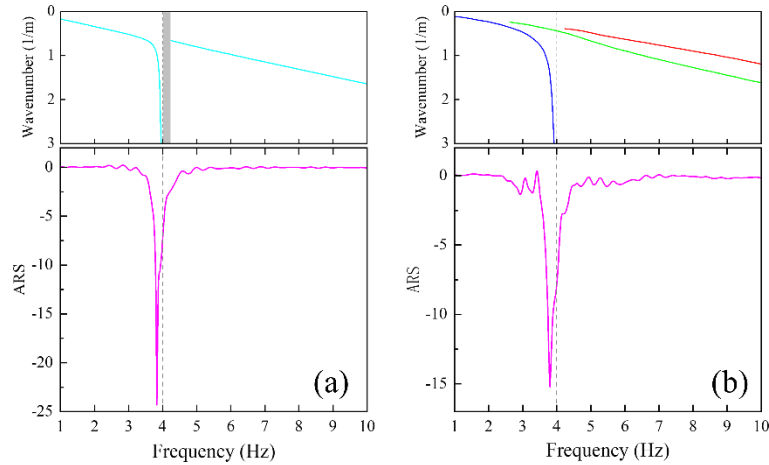
451 **4.2 Harmonic analysis**

452 **4.2.1 Frequency domain**

453
 454 In this section, the transmission efficiency of a finite number of surface resonators based on harmonic analysis is
 455 performed to validate the dispersion analysis predictions and obtain further insight into the attenuation performance
 456 of the stratified soil–resonator interaction.

457
 458 The ARS and corresponding dispersion curves for surface resonators arranged on the surface of homogeneous and
 459 stratified soil configurations were calculated (see Figure 8), respectively, to assess the attenuation performance of
 460 the metasurfaces. Figure 8(a) shows a significant acceleration amplitude attenuation near the resonant frequency
 461 owing to the local resonance or wave hybridization mechanism. As initially proposed by Boechler et al.⁵¹ and later
 462 by Palermo et al.,^{33,46} within the frequency band gap (gray shaded area in Figure 8(a)), Equation (39) has no real
 463 mathematical root and the corresponding solutions exist in the region below the shear wave (solid green line in
 464 Figure 9(a)) in the form of hybrid Rayleigh waves. The incident Rayleigh waves near the resonant frequency are
 465 either captured by the resonant metasurfaces or forced to propagate downward as hybrid Rayleigh waves with
 466 different phase velocities, thus reducing ground motion. Simultaneously, the offset phenomenon of the attenuation
 467 peak can be explained by the previous studies wherein Rayleigh waves and hybrid Rayleigh waves have been poorly
 468 coupled at the metasurfaces.^{32,46} Similarly, a prominent peak reduction can also be observed near the metasurface
 469 resonance in Figure 8(b) that can be attributed to the confinement of the first-order surface mode.

470



471
472

473 **Figure 8. Analytical dispersion curves and corresponding transmission spectra under different soil types. (a)**
474 **homogeneous soil and (b) stratified soil.**

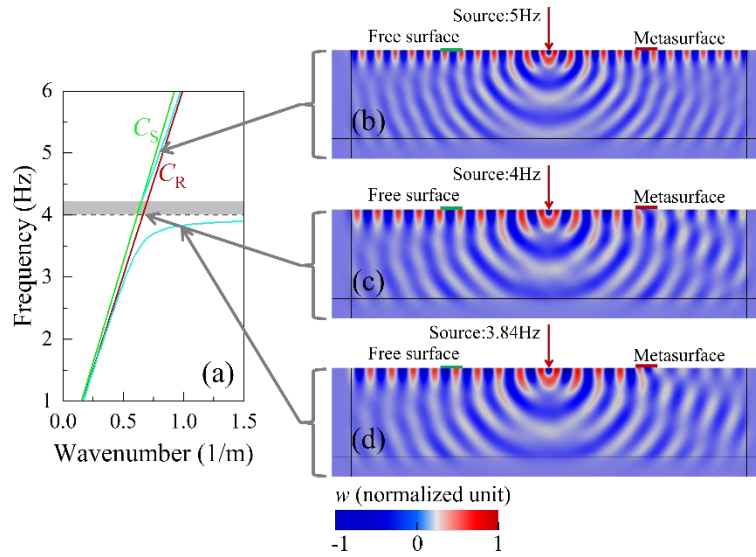
475

476 Moreover, the harmonic responses (vertical displacement fields) of homogeneous and stratified soil systems with
477 and without metasurfaces are plotted in Figure 9 and 10, respectively. Specifically, Figure 9(b), (c), and (d) present
478 the nephograms of the vertical displacement field generated by harmonic excitation at 3.84 Hz, 4 Hz, and 5 Hz. It
479 can be observed that the incident Rayleigh waves near the resonant frequency (that is, 3.84 Hz and 4 Hz) cause a
480 strong local resonance, resulting in a π phase shift of the incident waves that is converted into shear waves at the
481 metasurface edges and transferred to the underground. In contrast, the vertical displacement field generated by
482 harmonic excitation at 5 Hz (see Figure 9(b)) is basically consistent with the reference model on the left,
483 demonstrating that Rayleigh waves outside the band gap can propagate through the metasurfaces.

484

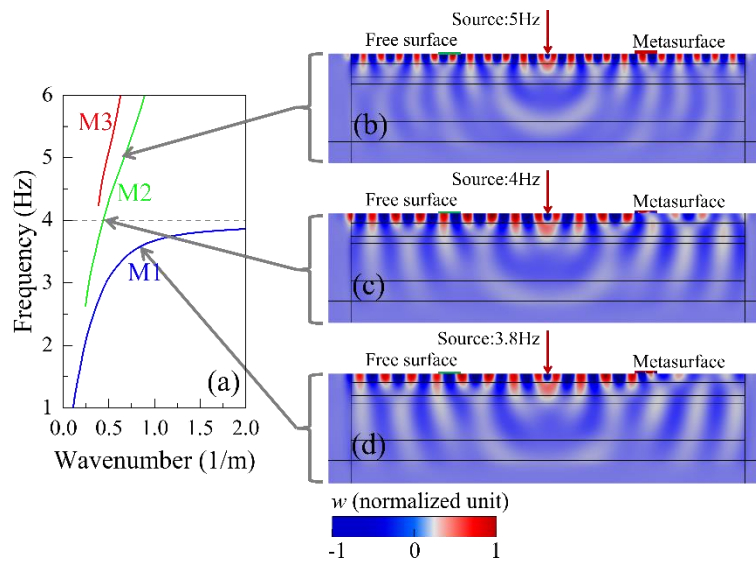
485 Regarding the stratified soil–resonator configuration, it can be found from Figure 10(b), (c), and (d) that most of the
486 wave energy is concentrated in the first layer because of the reflection of the elastic wave at the interface. However,
487 this peculiar soil stratification and stiffness profile have a negligible effect on the trapping ability of the resonant
488 metasurfaces. Considering the vertical displacement field under 3.8 Hz harmonic excitation as an example, the local
489 resonance of the surface resonators can still capture most of the wave energy, leading to the reduction of ground
490 vibration within a finite length behind the metasurfaces, as shown in Figure 10(d). For comparison, we also present
491 the vertical displacement field of a stratified soil system with and without metasurfaces at 5 Hz, as plotted in Figure
492 9(b). No apparent phenomena such as surface wave–resonance interaction and surface-to-shear wave conversion
493 were observed.

494



495
496
497
498
499
500
501

Figure 9. (a) Magnification of the dispersion curves of a homogeneous soil system coupled with resonant metasurfaces. The dispersion relation for both the shear wave (solid green line) and Rayleigh wave (solid red line) in the homogeneous elastic half-space are also superimposed in panel (a). (b) The nephogram of vertical displacement field generated by harmonic excitation at 3.84 Hz, 4 Hz, and 5 Hz.

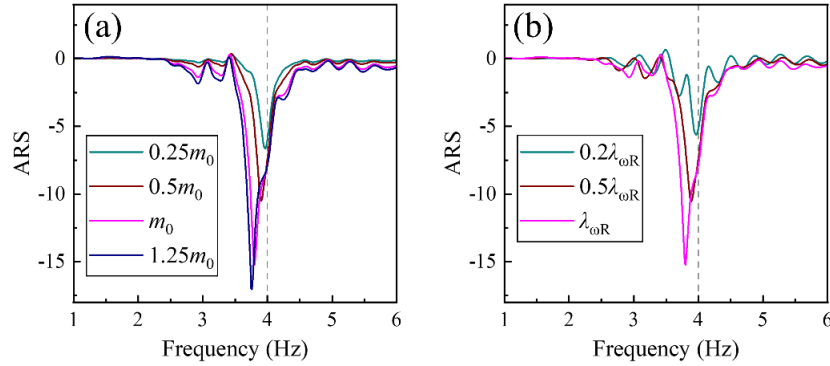


502
503
504
505
506
507
508
509

Figure 10. (a) Magnification of the dispersion curves of stratified soil-resonator interaction and (b) nephogram of vertical displacement field generated by harmonic excitation at 3.84 Hz, 4 Hz, and 5 Hz.

Parametric analyses, including resonator mass m_0 and arrangement length l_{bar} , were performed to investigate the attenuation capabilities of the metasurfaces. Keeping the resonance frequency of the resonator unchanged, Figure 11(a) presents the attenuation performance of the surface resonators with different masses. It is observed that both

510 the attenuation peak and starting frequency shift to lower frequencies, resulting in a larger attenuation domain for the
511 surface resonator. Therefore, increasing the resonator mass can widen the ARS and thus induce more broadband
512 performance for the metasurfaces. Simultaneously, another parametric study with different metasurface lengths was
513 conducted to assess the minimum surface wave barrier length required for significant ground attenuation. We
514 performed transmission analyses with different lengths of $0.2 \lambda_{\omega R}$, $0.5 \lambda_{\omega R}$, and $\lambda_{\omega R}$, and with a constant mass $m_0 =$
515 400 kg and $k_0 = 2.5266 \times 10^5 \text{ N/m}$ for each resonator, as shown in Figure 11(b). As expected, the vertical
516 acceleration responses at the output area decreased significantly as the metasurface length increased. In particular,
517 for a metasurface length of $l_{\text{bar}} = 0.5 \lambda_{\omega R}$, an approximately 30% reduction (that is, $\text{ARS} = -10$) of surface ground
518 motion is observed, indicating adequate attenuation performance of surface resonators.
519



520
521
522 **Figure 11. Effects of different parameters on acceleration reduction spectra. (a) Resonator mass (in this study,**
523 **$m_0 = 400 \text{ kg}$) and (b) Metasurface distribution length.**

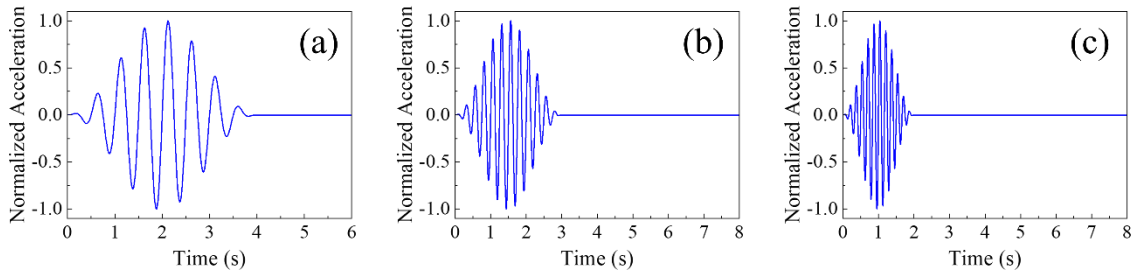
524
525 **4.2.2 Time domain**
526

527 Time-transient harmonic numerical simulations were also performed to further validate the numerical predictions of
528 the dispersion analyses and to investigate the wave attenuation capability of vertical oscillators near resonance. In
529 order to avoid undesired wave reflection, low reflection boundary conditions (LRBCs) are applied to the outside of
530 the PML layers that are proven to be more effective in absorbing the propagating shear and longitudinal waves at the
531 truncated boundaries in transient analysis.³⁷ Simultaneously, the bottom corners of the model are fixed, and three
532 input signals with 2 Hz, 4 Hz, and 6 Hz are considered (see Figure 12). Surface waves are excited at the source point
533 by utilizing a normalized harmonic acceleration in the z -direction. To avoid spurious oscillations at the onset, the
534 normalized acceleration amplitude is modulated by a Heaviside step function, as follows:

$$A_m = \begin{cases} \frac{1}{A_{\max}} \left[1 - \cos\left(\frac{2\pi f_c t}{C}\right) \right] \sin(2\pi f_c t) & \text{for } 0 \leq t < \frac{C}{f_c}, \\ 0 & \text{for } t \geq \frac{C}{f_c}. \end{cases} \quad (41)$$

535 where A_{\max} is the maximum signal amplitude, f_c is the central frequency of the applied pulses, C is the number of
536 wave cycles, and t is the time duration. Such excitation is chosen to highlight the isolation performance of the
537 designed metasurfaces, emphasizing that strong coupling occurs around the resonator resonance. In addition, the FE
538 model used for transient analysis was consistent with the description of the transmission model, as shown in Figure

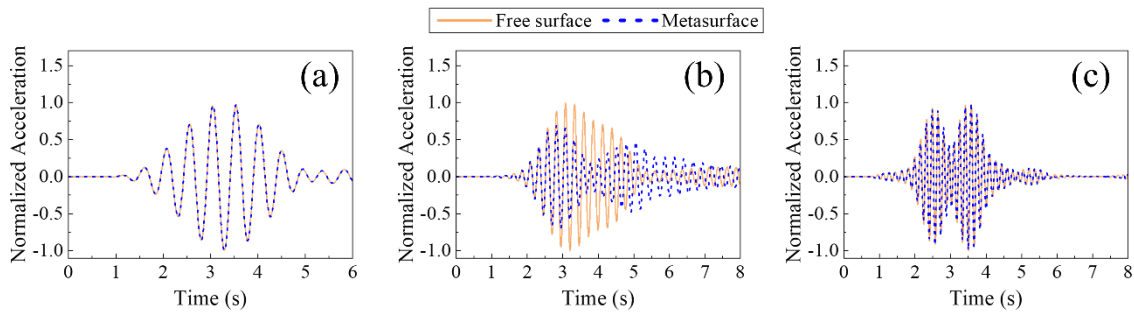
539 3.
540



541
542
543
544

Figure 12. Normalized input wave signal. (a) $f_c = 2$ Hz, $C = 8$; (b) $f_c = 4$ Hz, $C = 12$; and (c) $f_c = 6$ Hz, $C = 12$.

545 The normalized average vertical acceleration responses at the detection area (that is, Output 1 and Output 2) were
546 recorded and compared, as shown in Figure 13. The dashed and solid lines denote the results obtained with and
547 without metasurfaces, respectively. As shown in Figure 13(b), the vertical acceleration responses at the output
548 domain with metasurfaces are significantly smaller than those of signals without metasurfaces, owing to the
549 generation of local resonance. When the center frequency of the input signal $f_c = 4$ Hz, the average vertical
550 acceleration amplitude decreases by approximately 30% compared with the reference free surface. The output
551 signals far from the resonant frequencies are plotted, as shown in Figure 13(a) and (c). It can be observed that the
552 amplitudes of the time transient acceleration at the detection area are almost the same in both configurations (with
553 and without resonators). Again, the transient analysis results confirm that the considerable amplitude reduction
554 observed around the resonant frequency is caused by the strong coupling between the surface waves and
555 metasurfaces.
556



557
558
559
560
561

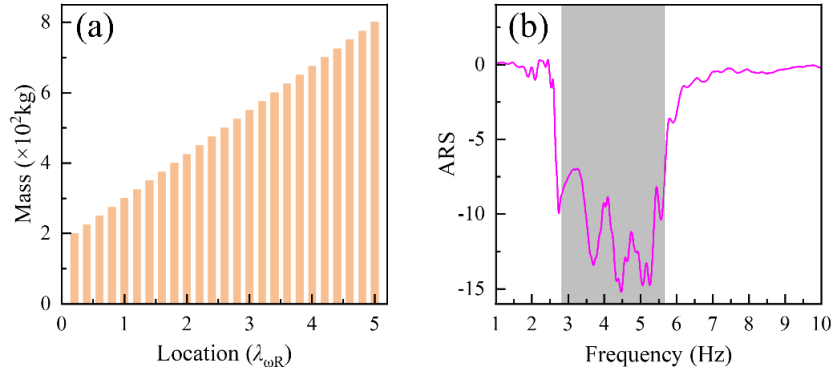
Figure 13. Normalized average vertical acceleration response at the output area. (a) $f_c = 2$ Hz, $C = 5$; (b) $f_c = 4$ Hz, $C = 12$; (c) $f_c = 5$ Hz, $C = 10$; and (d) $f_c = 12$ Hz, $C = 12$.

562 4.3 Attenuation efficiency of a graded metasurface

563
564
565
566

As mentioned above, the resonance frequencies of the metasurface were reasonably tailored to achieve considerable attenuation. To obtain attenuation at ultralow frequencies and a wider frequency range, the classic gradient metawedge presented by Colombi and Colquitt et al.³¹ with decreasing frequencies along the propagation direction

567 is reconsidered. Note that a decreasing frequency metasurface can be modeled by linearly modifying the mass or
 568 spring stiffness of the vertical oscillators. Therefore, a decreasing-frequency case is adopted by linearly increasing
 569 the masses from 200 to 800 kg and maintaining the spring stiffness k_0 at 2.5266×10^5 , as depicted in Figure 14(a).
 570 Figure 14(b) displays the acceleration attenuation spectra of the gradient metasurfaces in the frequency range of
 571 1–10 Hz. The shaded area represents the corresponding resonance frequencies in the range of 2.82 Hz to 5.65 Hz. A
 572 wider attenuation zone and a more significant attenuation effect can be visually observed in the case of a resonant
 573 metasurface with a decreasing frequency compared with a constant frequency.
 574



575

576

577 **Figure 14. (a) Schematic of the mass distribution of graded metasurfaces for a constant stiffness of the**
 578 **resonators and (b) corresponding acceleration reduction spectra. The considered graded metasurfaces have a**
 579 **length $l_{\text{bar}} = 5\lambda_{\omega R}$ and stiffness $k_0 = 2.5266 \times 10^5$ N/m.**

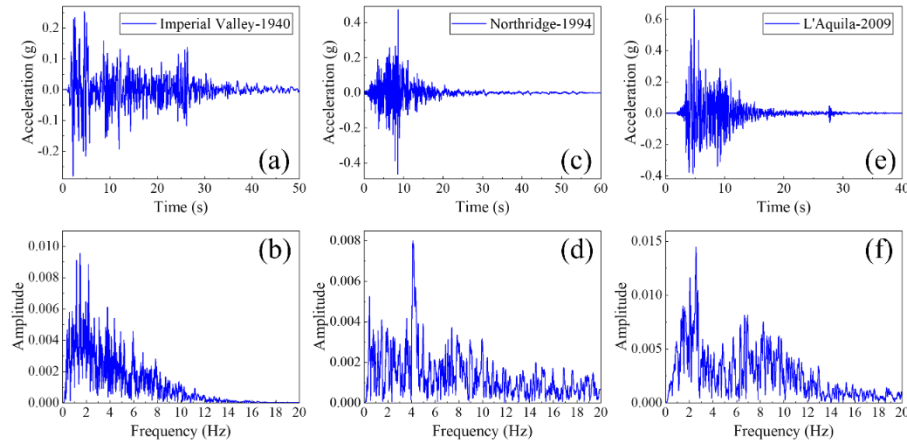
580

581 Furthermore, it is important to scrutinize the attenuation effect of the graded resonant metasurfaces via time-domain
 582 analyses with a natural seismic acceleration record. Thus, three accelerograms recorded from the Pacific Earthquake
 583 Engineering Research Ground Motion Database⁵² were selected: Imperial Valley, Northridge, and L’Aquila as
 584 seismic inputs. Figure 15 depicts the time history and corresponding Fourier spectra of the three ground vibrations.
 585 Figure 15(b) shows that the dominant frequencies of the Imperial Valley earthquake are in the range of 1–6 Hz that
 586 is consistent with the attenuation zones of the graded metasurfaces and is expected to achieve significant shielding
 587 performance. However, the main frequency bands of the other two seismic records are relatively scattered, and there
 588 are still large vibration amplitudes in the frequency bands outside the attenuation zone (for example, 6–10 Hz) that
 589 makes it difficult to achieve attenuation.

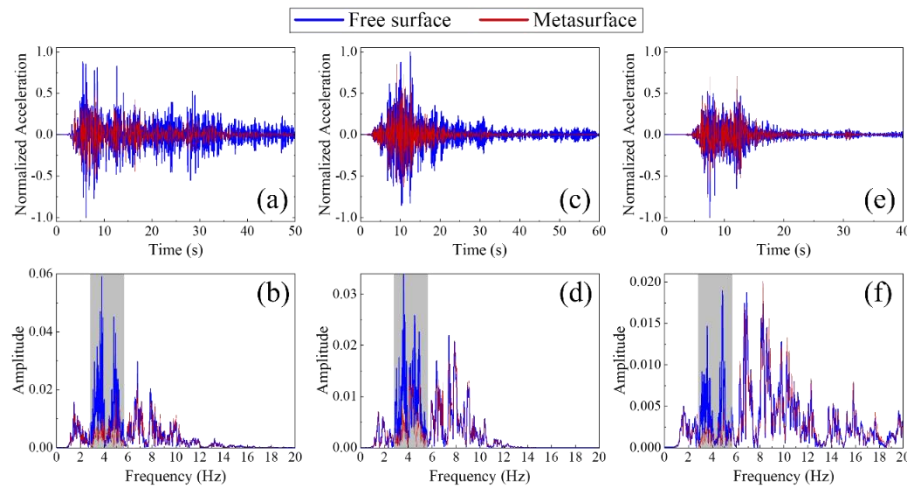
590

591 Time history analyses were performed by applying seismic inputs directly to the source location. For the FE models
 592 with or without graded metasurfaces, the average acceleration responses in the vertical direction were calculated in
 593 the detection area. After the acquisition, fast Fourier transform was applied to the output responses, and their
 594 frequency components were compared to highlight the attenuation effect in the decreasing-frequency case. Figure 16
 595 displays the normalized average vertical acceleration responses and corresponding Fourier spectra at the output area,
 596 considering the presence or absence of graded metasurfaces. It can be found that the vertical acceleration amplitude
 597 in the FE model with graded metasurfaces (denoted as solid red lines) is reduced by 39%, 27%, and 25%,
 598 respectively, compared with those in the reference model (denoted as solid blue lines). Simultaneously, the

599 corresponding frequency components at Output 1 (graded metasurface), as shown in Figure 16(b), (d), and (f) are
 600 significantly reduced in the attenuation zone compared with those at Output 2 (free surface). In conclusion, the
 601 above results once again prove that the tuned resonant metasurfaces can achieve broadband surface wave attenuation
 602 and are expected to effectively avoid seismic damage to critical infrastructures.
 603



604
 605 **Figure 15. Input seismic wave acceleration records and corresponding Fourier spectra. (a, b) Imperial Valley**
 606 **earthquake; (c, d) Northridge earthquake and (e, f) L'Aquila earthquake.⁵²**
 607



608
 609
 610 **Figure 16. Normalized average vertical acceleration response at the output area and corresponding Fourier**
 611 **spectra with and without metasurfaces. (a, b) Imperial Valley earthquake; (c, d) Northridge earthquake; and**
 612 **(e, f) L'Aquila earthquake.**

614 **5 CONCLUSIONS**

615
 616 The recent proliferation of resonant metamaterials developed for seismic wave shielding is based on stimulated
 617 theoretical and analytical frameworks capable of describing the interaction of surface waves with longitudinal
 618 resonance metasurfaces. Within this context, this study theoretically investigates the dispersion properties in the

619 actual site conditions by considering the coupling of Rayleigh waves with metasurfaces attached to the free surface
620 of a stratified semi-infinite space. The dispersion curves of the three configurations, including a stratified soil system,
621 a homogeneous soil–resonator coupling system, and a stratified soil–resonator coupling system, were obtained by
622 numerical simulations. Additionally, a finite-length metasurface and a graded resonant metasurface with decreasing
623 frequency were used to evaluate the attenuation efficiency in the frequency domain and time domain, respectively.
624 The main findings of this study are summarized as follows:

625

626 (1) The analytical framework is developed by introducing the classical elastodynamics theory and an
627 effective medium description to investigate the eigen equation of Raleigh waves propagating through
628 periodically distributed vertical resonators in multiple stratified soil substrates. Simultaneously, the
629 improved matrix algorithm proposed in this study can be used to calculate the dispersion relations of
630 stratified soil–resonator interactions promptly and accurately, avoiding the problem of high-frequency
631 effective digit loss.

632 (2) The analytical and numerical solutions of the dispersion curves are in good agreement that validates the
633 feasibility of the Bloch-wave FE method. It is observed that the first-order surface mode gradually
634 becomes a flat dispersive branch near the metasurface resonance, while the other higher-order surface
635 modes still cross the surface wave band gap. Thus, it is highlighted that only the first-order mode is
636 strongly coupled with the resonant metasurfaces, and the effect of the higher-order modes is negligible.

637 (3) The results of harmonic analyses show that the transmission model with a finite-length metasurface
638 exhibits a sharp attenuation in a narrow frequency range near resonance. In addition, the coupling degree
639 of Rayleigh waves and hybrid Rayleigh waves at the soil–resonator interface is sensitive to the resonator
640 mass m_0 . Broadband attenuation can be achieved by increasing the resonator mass or metasurface length
641 within a certain range.

642 (4) By reasonably adjusting the resonator mass or spring compression stiffness, it is possible to obtain a
643 graded metasurface with an ultra-low starting frequency and broadband attenuation. In particular, it is
644 found that the vertical acceleration amplitude in the output region of the FE model with a graded resonant
645 metasurface can be reduced by 39% relative to the reference model.

646

647 As mentioned above, the actual site conditions are far more complex than the stratified case assumed in this paper;
648 for example, weak interbeds and groundwater are common in practice. Moreover, the failure of soil bearing capacity
649 caused by the large resonating masses should be checked according to real site conditions. Further research efforts
650 will be devoted to develop 3D resonant metasurfaces and investigate the resonators damping, soil nonlinearity, and
651 activation time of the resonant metasurfaces on the shielding effect. One can expect a substantial volume of
652 quantitative studies on seismic metabarriers using realistic materials and structural parameters in the coming years.

653

654 REFERENCES

655

- 656 1. Hussein MI, Leamy MJ, Ruzzene M. Dynamics of Phononic Materials and Structures: Historical Origins,
657 Recent Progress, and Future Outlook. *Appl Mec Rev* 2014;66(4):040802.
- 658 2. Yablonovitch E. Inhibited Spontaneous Emission in Solid-State Physics and Electronics. *Phys Rev Lett*
659 1987;58(20):2059–2062.

- 660 3. John S. Strong localization of photons in certain disordered dielectric superlattices. *Phys Rev Lett*
661 1987;58(23):2486–2489.
- 662 4. Kushwaha MS, Halevi P, Dobrzynski L, Djafari-Rouhani B. Acoustic band structure of periodic elastic
663 composites. *Phys Rev Lett* 1993;71(13):2022–2025.
- 664 5. Liu Z. Locally Resonant Sonic Materials. *Science* 2000;289(5485):1734–1736.
- 665 6. Zhang X, Liu Z. Negative refraction of acoustic waves in two-dimensional phononic crystals. *Appl Phys Lett*
666 2004;85(2):341–343.
- 667 7. Sukhovich A, Jing L, Page JH. Negative refraction and focusing of ultrasound in two-dimensional phononic
668 crystals. *Phys Rev B* 2008;77(1):014301.
- 669 8. Kan W, Shen Z. Ultra-transparent media with anisotropic mass density for broadband acoustic invisibility. *Appl*
670 *Phys Lett* 2017;111(22):223501.
- 671 9. Zhu J, Chen T, Song X, Chen C, Liu Z, Zhang J. Three-dimensional large-scale acoustic invisibility cloak with
672 layered metamaterials for underwater operation. *Phys Scripta* 2019;94(11):115003.
- 673 10. Sukhovich A, Merheb B, Muralidharan K, Vasseur JO, Pennec Y, Deymier PA, et al. Experimental and
674 Theoretical Evidence for Subwavelength Imaging in Phononic Crystals. *Phys Rev Lett* 2009;102(15):154301.
- 675 11. Bak AO, Giannini V, Maier SA, Phillips CC. Super-resolution with a positive epsilon multi-quantum-well
676 super-lens. *Appl Phys Lett* 2013;103(26):261110.
- 677 12. Tsung-Tsong Wu, Jin-Chen Hsu, Jia-Hong Sun. Phononic plate waves. *IEEE T Ultrason Ferr*
678 2011;58(10):2146–2161.
- 679 13. Thota M, Wang KW. Tunable waveguiding in origami phononic structures. *J Sound Vib* 2018;430(1):93–100.
- 680 14. Muzar E, Aval GA, Stotz JAH. Wet-etched phononic crystal waveguiding on GaAs. *J Phys D Appl Phys*
681 2018;51(4):044001.
- 682 15. Chen H, Chan CT. Acoustic cloaking and transformation acoustics. *J Phys D Appl Phys* 2010;43(11):113001.
- 683 16. Brun M, Guenneau S, Movchan AB. Achieving control of in-plane elastic waves. *Appl Phys Lett*
684 2009;94(6):061903.
- 685 17. Chen H, Chan CT. Acoustic cloaking in three dimensions using acoustic metamaterials. *Appl Phys Lett*
686 2007;91(18):183518.
- 687 18. Chen YY, Barnhart MV, Chen JK, Hu GK, Sun CT, Huang GL. Dissipative elastic metamaterials for broadband
688 wave mitigation at subwavelength scale. *Compos Struct* 2016;136:358–371.
- 689 19. Gonella S, To AC, Liu WK. Interplay between phononic bandgaps and piezoelectric microstructures for energy
690 harvesting. *J Mech Phys Solids* 2009;57(3):621–633.
- 691 20. Miniaci M, Krushynska A, Bosia F, Pugno NM. Large scale mechanical metamaterials as seismic shields. *New*
692 *J Phys* 2016;18(8):083041.
- 693 21. Basone F, Wenzel M, Bursi OS, Fossetti M. Finite locally resonant Metafoundations for the seismic protection
694 of fuel storage tanks. *Earthq Eng Struct D* 2019;48(2):232–252.
- 695 22. Brûlé S, Javelaud EH, Enoch S, Guenneau S. Experiments on Seismic Metamaterials: Molding Surface Waves.
696 *Phys Rev Lett* 2014;112(13):133901.
- 697 23. Zhao C, Zeng C, Huang H, Dai J, Bai W, Wang J, et al. Preliminary study on the periodic base isolation
698 effectiveness and experimental validation. *Eng Struct* 2021;226(7):111364.
- 699 24. Zhao C, Zeng C, Witarto W, wen Huang H, Dai J, Mo YL. Isolation performance of a small modular reactor
700 using 1D periodic foundation. *Eng Struct* 2021;244(9–10):112825.

- 701 25. Leonhardt U. Optical Conformal Mapping. *Science* 2006;312(5781):1777–1780.
- 702 26. Pendry JB. Controlling Electromagnetic Fields. *Science* 2006;312(5781):1780–1782.
- 703 27. Yu JK, Mitrovic S, Tham D, Varghese J, Heath JR. Reduction of thermal conductivity in phononic nanomesh
704 structures. *Nat Nanotechnol* 2010;5(10):718–721.
- 705 28. Cheng ZB, Shi ZF. Composite periodic foundation and its application for seismic isolation. *Earthq Eng Struct*
706 *D* 2018;47(4):925–944.
- 707 29. Xiang HJ, Shi ZF, Wang SJ, Mo YL. Periodic materials-based vibration attenuation in layered foundations:
708 experimental validation. *Smart Mater Struct* 2012;21(11):112003.
- 709 30. Colombi A, Roux P, Guenneau S, Gueguen P, Craster RV. Forests as a natural seismic metamaterial: Rayleigh
710 wave bandgaps induced by local resonances. *Sci Rep* 2016;6(1):19238.
- 711 31. Colombi A, Colquitt D, Roux P, Guenneau S, Craster RV. A seismic metamaterial: The resonant metawedge. *Sci*
712 *Rep* 2016;6(1):27717.
- 713 32. Colquitt DJ, Colombi A, Craster RV, Roux P, Guenneau SRL. Seismic metasurfaces: Sub-wavelength
714 resonators and Rayleigh wave interaction. *J Mech Phys Solids* 2017;99:379–393.
- 715 33. Palermo A, Krödel S, Marzani A, Daraio C. Engineered metabarrier as shield from seismic surface waves. *Sci*
716 *Rep* 2016;6(1):39356.
- 717 34. Liu C heng, Nagel SR. Sound in sand. *Phys Rev Lett* 1992;68(15):2301–2304.
- 718 35. Palermo A, Krödel S, Matlack KH, Zaccherini R, Dertimanis VK, Chatzi EN, et al. Hybridization of Guided
719 Surface Acoustic Modes in Unconsolidated Granular Media by a Resonant Metasurface. *Phys Rev Appl*
720 2018;9(5):054026.
- 721 36. Zaccherini R, Palermo A, Marzani A, Colombi A, Dertimanis V, Chatzi E. Mitigation of Rayleigh-like waves in
722 granular media via multi-layer resonant metabarriers. *Appl Phys Lett* 2020;117(25):254103.
- 723 37. Zeighami F, Palermo A, Vratsikidis A, Cheng Z, Pitilakis D, Marzani A. Medium-scale resonant wave barrier
724 for seismic surface waves. *Mech Based Des Struc* 2020:1–16.
- 725 38. Pu X, Palermo A, Cheng Z, Shi Z, Marzani A. Seismic metasurfaces on porous layered media: Surface
726 resonators and fluid-solid interaction effects on the propagation of Rayleigh waves. *Int J Eng Sci*
727 2020;154:103347.
- 728 39. Graff KF. *Wave motion in elastic solids*. Revised edition. New York: Dover Publications; 1991.
- 729 40. Kushwaha MS, Halevi P, Martínez G, Dobrzynski L, Djafari-Rouhani B. Theory of acoustic band structure of
730 periodic elastic composites. *Phys Rev B* 1994;49(4):2313–2322.
- 731 41. Knopoff L. A matrix method for elastic wave problems. *B Seismol Soc Am* 1964;54(1):431–438.
- 732 42. Dunkin JW. Computation of modal solutions in layered, elastic media at high frequencies. *B Seismol Soc Am*
733 1965;55(2):335–358.
- 734 43. Thrower EN. The computation of the dispersion of elastic waves in layered media. *J Sound Vib*
735 1965;2(3):210–226.
- 736 44. Abo-Zena A. Dispersion function computations for unlimited frequency values. *Geophys J Int*
737 1979;58(1):91–105.
- 738 45. Cai C, Gao L, He X, Zou Y, Yu K, Wu D. The surface wave attenuation zone of periodic composite in-filled
739 trenches and its isolation performance in train-induced ground vibration isolation. *Comput Geotech*
740 2021;139:104421.
- 741 46. Palermo A, Vitali M, Marzani A. Metabarriers with multi-mass locally resonating units for broad band Rayleigh

- 742 waves attenuation. *Soil Dyn Earthq Eng* 2018;113:265–277.
- 743 47. Moser F, Jacobs LJ, Qu J. Modeling elastic wave propagation in waveguides with the finite element method.
744 *Ndt&e Int* 1999;32(4):225–234.
- 745 48. De Marchi L, Marzani A, Miniaci M. A dispersion compensation procedure to extend pulse-echo defects
746 location to irregular waveguides. *Ndt&e Int* 2013;54:115–122.
- 747 49. Phani AS, Woodhouse J, Fleck NA. Wave propagation in two-dimensional periodic lattices. *J Acoust Soc Am*
748 2006;119(4):1995–2005.
- 749 50. Huang J, Liu W, Shi Z. Surface-wave attenuation zone of layered periodic structures and feasible application in
750 ground vibration reduction. *Constr Build Mater* 2017;141:1–11.
- 751 51. Boechler N, Eliason JK, Kumar A, Maznev AA, Nelson KA, Fang N. Interaction of a Contact Resonance of
752 Microspheres with Surface Acoustic Waves. *Phys Rev Lett* 2013;111(3):036103.
- 753 52. Pacific Earthquake Engineering Research Center. <https://ngawest2.berkeley.edu/>

754

755 **APPENDIX: Definition of the matrix elements**

756

757 The matrix \mathbf{H} is:

$$\mathbf{H} = \begin{bmatrix} 1 & 1 & \gamma_s & \gamma_s \\ \gamma_L & -\gamma_L & 1 & -1 \\ \rho(\gamma-1) & \rho(\gamma-1) & \rho\gamma_s & \rho\gamma_s \\ \rho\gamma_L & -\rho\gamma_L & \rho(\gamma-1) & -\rho(\gamma-1) \end{bmatrix}. \quad (\text{A1})$$

758

759 The matrix \mathbf{H}^{-1} is

$$\mathbf{H}^{-1} = \frac{1}{2} \begin{bmatrix} \gamma & -\frac{\gamma-1}{\gamma_L} & -\frac{1}{\rho} & \frac{1}{\rho\gamma_L} \\ \gamma & \frac{\gamma-1}{\gamma_L} & -\frac{1}{\rho} & -\frac{1}{\rho\gamma_L} \\ -\frac{\gamma-1}{\gamma_s} & \gamma & \frac{1}{\rho\gamma_s} & -\frac{1}{\rho} \\ -\frac{\gamma-1}{\gamma_s} & -\gamma & \frac{1}{\rho\gamma_s} & \frac{1}{\rho} \end{bmatrix}. \quad (\text{A2})$$

760

761 The matrix \mathbf{E}_m^* is:

$$\mathbf{E}_m^* = \text{diag} \left[1 \quad PQ \quad \frac{P}{Q} \quad \frac{Q}{P} \quad \frac{1}{PQ} \quad 1 \right]. \quad (\text{A3})$$

762

763 The elements of matrix \mathbf{H}_m^* are:

$$\begin{aligned} h_{11}^* &= -2\gamma_L & h_{12}^* &= 1 - \gamma_L\gamma_s & h_{13}^* &= -1 - \gamma_L\gamma_s \\ h_{14}^* &= 1 + \gamma_L\gamma_s & h_{15}^* &= -1 + \gamma_L\gamma_s & h_{16}^* &= -2\gamma_s \end{aligned} \quad (\text{A4})$$

$$\begin{array}{lll}
h_{21}^* = 0 & h_{22}^* = \rho\gamma_s & h_{23}^* = \rho\gamma_s \\
h_{24}^* = \rho\gamma_s & h_{25}^* = \rho\gamma_s & h_{26}^* = 0 \\
h_{31}^* = -2\rho\gamma_L & h_{32}^* = \rho(\gamma-1) - \rho\gamma_L\gamma_s & h_{33}^* = -\rho(\gamma-1) - \rho\gamma_L\gamma_s \\
h_{34}^* = \rho(\gamma-1) + \rho\gamma_L\gamma_s & h_{35}^* = -\rho(\gamma-1) + \rho\gamma_L\gamma_s & h_{36}^* = -2\rho\gamma_s(\gamma-1) \\
h_{41}^* = 2\rho\gamma_L(\gamma-1) & h_{42}^* = \rho\gamma_L\gamma_s - \rho(\gamma-1) & h_{43}^* = \rho\gamma_L\gamma_s + \rho(\gamma-1) \\
h_{44}^* = -\rho\gamma_L\gamma_s - \rho(\gamma-1) & h_{45}^* = -\rho\gamma_L\gamma_s + \rho(\gamma-1) & h_{46}^* = 2\rho\gamma_s \\
h_{51}^* = 0 & h_{52}^* = -\rho\gamma_L & h_{53}^* = \rho\gamma_L \\
h_{54}^* = \rho\gamma_L & h_{55}^* = -\rho\gamma_L & h_{56}^* = 0 \\
h_{61}^* = -2\rho^2\gamma_L(\gamma-1) & h_{62}^* = \rho^2(\gamma-1)^2 - (\rho\gamma)^2\gamma_L\gamma_s & h_{63}^* = -\rho^2(\gamma-1)^2 - (\rho\gamma)^2\gamma_L\gamma_s \\
h_{64}^* = \rho^2(\gamma-1)^2 + (\rho\gamma)^2\gamma_L\gamma_s & h_{65}^* = -\rho^2(\gamma-1)^2 + (\rho\gamma)^2\gamma_L\gamma_s & h_{66}^* = -2\rho^2\gamma_s(\gamma-1)
\end{array}$$

764

765 The elements of matrix $(\mathbf{H}_m^{-1})^*$ are:

$$\begin{array}{llll}
H_{11}^* = -\frac{2\gamma(\gamma-1)}{\gamma_L} & H_{12}^* = 0 & H_{13}^* = -\frac{2\gamma}{\rho\gamma_L} & H_{14}^* = \frac{2(\gamma-1)}{\rho\gamma_L} \\
H_{15}^* = 0 & H_{16}^* = \frac{2}{\rho^2\gamma_L} & H_{21}^* = \gamma^2 - \frac{(\gamma-1)^2}{\gamma_L\gamma_s} & H_{22}^* = \frac{1}{\rho\gamma_s} \\
H_{23}^* = -\frac{\gamma}{\rho} + \frac{\gamma-1}{\rho\gamma_L\gamma_s} & H_{24}^* = \frac{\gamma}{\rho} - \frac{\gamma-1}{\rho\gamma_L\gamma_s} & H_{25}^* = -\frac{1}{\rho\gamma_L} & H_{26}^* = \frac{1}{\rho^2} - \frac{1}{\rho^2\gamma_L\gamma_s} \\
H_{31}^* = -\gamma^2 - \frac{(\gamma-1)^2}{\gamma_s\gamma_L} & H_{32}^* = \frac{1}{\rho\gamma_s} & H_{33}^* = \frac{\gamma}{\rho} + \frac{\gamma-1}{\rho\gamma_L\gamma_s} & H_{34}^* = -\frac{\gamma}{\rho} - \frac{\gamma-1}{\rho\gamma_L\gamma_s} \\
H_{35}^* = \frac{1}{\rho\gamma_L} & H_{36}^* = -\frac{1}{\rho^2} - \frac{1}{\rho^2\gamma_L\gamma_s} & H_{41}^* = \gamma^2 + \frac{(\gamma-1)^2}{\gamma_L\gamma_s} & H_{42}^* = \frac{1}{\rho\gamma_s} \\
H_{43}^* = -\frac{\gamma}{\rho} - \frac{\gamma-1}{\rho\gamma_L\gamma_s} & H_{44}^* = \frac{\gamma}{\rho} + \frac{\gamma-1}{\rho\gamma_L\gamma_s} & H_{45}^* = \frac{1}{\rho\gamma_L} & H_{46}^* = \frac{1}{\rho^2} + \frac{1}{\rho^2\gamma_L\gamma_s} \\
H_{51}^* = -\gamma^2 + \frac{(\gamma-1)^2}{\gamma_L\gamma_s} & H_{52}^* = \frac{1}{\rho\gamma_s} & H_{53}^* = \frac{\gamma}{\rho} - \frac{\gamma-1}{\rho\gamma_L\gamma_s} & H_{54}^* = -\frac{\gamma}{\rho} + \frac{\gamma-1}{\rho\gamma_L\gamma_s} \\
H_{55}^* = -\frac{1}{\rho\gamma_L} & H_{56}^* = -\frac{1}{\rho^2} + \frac{1}{\rho^2\gamma_L\gamma_s} & H_{61}^* = \frac{2\gamma(\gamma-1)}{\gamma_s} & H_{62}^* = 0 \\
H_{63}^* = -\frac{2(\gamma-1)}{\rho\gamma_s} & H_{64}^* = \frac{2\gamma}{\rho\gamma_s} & H_{65}^* = 0 & H_{66}^* = \frac{2}{\rho^2\gamma_s}
\end{array} \tag{A5}$$

766